
INTERPLAY OF NONSMOOTHNESS, TIME DELAY, AND STOCHASTICITY IN TURNING DYNAMICS

✉ Meiyazhagan Jaganathan¹, ✉ Vikram Pakrashi¹, and ✉ Aasifa Rounak*¹

¹UCD Centre for Mechanics, Dynamical Systems and Risk Laboratory, School of Mechanical and Materials Engineering, University College Dublin, D04 V1W8, Dublin, Ireland

ABSTRACT

The stochastic dynamics of orthogonal metal cutting with both regenerative and nonsmooth frictional effects are investigated numerically in this paper. The shortcomings of neglecting nonsmoothness in frictional and stochastic effects in modeling the dynamics of such a machining process are demonstrated. Dynamics of the tool motion is observed to exhibit rich nonlinear phenomena such as stick-slip during chatter, with stochastic perturbations in cutting forces adding further complexity, leading to the occurrence of stochastic P and D bifurcations. Measures of entropy are found to be effective in quantifying the dynamical transitions occurring in the dynamics of the tool. Subsequently, basin stability analyses, modified to account for stochasticity and time-delays, are carried out to systematically investigate the dynamics of the cutting tool across multiple surface roughness profiles of the workpiece. Basin stability analyses indicate that chatter can be controlled by restricting initial tool displacement and controlling initial workpiece surface roughness, suggesting practical strategies to improve machining outcomes for precision manufacturing.

Keywords Frictional Chatter, Stick-slip, Stochastic bifurcations, Multistability, Metal Cutting

1 Introduction

Nonsmooth dynamical systems are essential for modeling physical processes with discontinuities, impacts, or switching events [1]. In mechanical systems, these phenomena often result from contact [2], friction, and intermittent engagement [3], causing abrupt transitions in forces and system responses. Metal cutting is one such important area of application where nonsmooth effects become dominant due to frictional effects or when the tool periodically establishes contact with the workpiece and disengages contact after a certain amount of time, leading to self-excited vibrations, such as chatter [4]. Chatter, the back-and-forth vibration of a tool against the workpiece surface, is a major problem for stable machining. It causes material waste, reduced surface quality, reduces tool life through wear and damage, exacerbates safety issues, including the generation of high-decibel noise, lowers productivity, and increases the cost of cutting processes. Despite advancements in Computer Numerical Control (CNC) technology, machine operations still face challenges from chatter [5].

Chatter is classified into four categories based on the source of the cutting instability: (i) frictional [6, 7], (ii) regenerative [8, 9], (iii) mode-coupling [10], and (iv) thermo-mechanical [11]. Among these, frictional and regenerative chatter have attracted significant attention in both nonlinear dynamics and manufacturing communities due to their frequent occurrence and most substantial influence on machining stability. Frictional chatter, also known as primary chatter, is driven by the velocity-dependent frictional effects at the interface between the rake face of the tool and the chip. Regenerative chatter, the secondary type, arises from waviness in the workpiece geometry resulting from prior passes, which affects the dynamics of subsequent passes, leading to higher cutting forces and dynamical instabilities [10]. Orthogonal metal cutting is susceptible to both frictional and regenerative effects.

*corresponding author - aasifa.rounak@ucd.ie

Orthogonal metal cutting is an extensively used machining technique for manufacturing, where a single-point cutting tool, oriented orthogonally with the workpiece, generates *chips* by removing material through shear deformation. Understanding and controlling the dynamics involved in orthogonal cutting, such as *turning* operations, is essential for improving machining efficiency and precision. Turning operations have been extensively studied in the past decades. Wiercigroch *et. al* [11] revisited classical and modern models of *chip formation* and cutting mechanics, emphasizing the importance of nonlinearities in understanding and predicting machining behavior. A two-degree-of-freedom (2-DOF) frictional model for the machine-tool and cutting process system was introduced in 2001 [6], where the authors explored the emergence of period-doubling bifurcations and chaotic dynamics in orthogonal metal cutting. In 2014, Rusinek *et. al*[7] improved the 2-DOF frictional model by incorporating the flank forces, demonstrating how *flank forces* play a major role in stable dynamics. Gábor Stépán's 2001 work [9] introduced a time-delay nonlinear model for regenerative turning, addressing the limitations of linear models and proposing a three-quarter power law for cutting forces. Investigation of the global dynamics of regenerative chatter in turning in the deterministic sense was presented by Wahi *et. al* [8], with particular focus on the phenomenon of self-interrupted cutting due to contact loss between tool and workpiece. A single-degree-of-freedom (SDOF) nonsmooth delay differential-algebraic equation was later introduced by Dombovari *et. al* [12] to analyze the chatter in regenerative orthogonal cutting. This study also employed DDE-BIFTOOL [13] to perform continuation analysis on the smooth version of the model.

Chip formation in orthogonal cutting has been studied for titanium alloys such as (Ti6Al4V) [14], and the influence of chip segmentation on the cutting stability has also been explored [15]. Additionally, the role of *process damping* in orthogonal cutting has received significant attention. Ahmadi [16] analytically modeled the process damping arising from flank contact. Eynian and Altintas [17] developed two models, with their advanced formulation explicitly modeling the process damping from flank wear, showing its stabilising effect. Similarly, Yuvaraju *et al* [18] introduced a 2-DOF nonlinear model for internal turning that includes flank-induced damping and frictional effects, capturing complex dynamics like internal resonance. Investigations into the chatter phenomenon have extended beyond turning and orthogonal cutting to encompass a wide range of machining processes. In *grinding*, studies have explored the onset and suppression of chatter under various grinding conditions [19–23]. In *drilling*, generalized models have been developed to study chatter stability [24–26]. *Boring* operations have also been analyzed for chatter stability, particularly in robotic boring systems [27]. *Milling*, one of the most extensively studied cutting processes, has seen the development of time-domain and frequency-domain models [28–30]. Additional complexity like chatter stability ([31]) is introduced for *Parallel Machining*, where multiple tools cut simultaneously. Further insights into these various investigations and a more comprehensive history of studies around the phenomenon of chatter can be found in several review articles [10, 32–34].

Most of these studies, representing a wide range of models exhibiting chatter, rely on delay differential equations (DDEs) based deterministic models where the machining parameters, including cutting force coefficients, typically rely on averaged constant values. As the majority of machining models in use at present are deterministic, insights obtained from such models are approximate, conservative, and even correspond to rules of thumb where stochastic aspects are relevant. The dynamic behaviour and stability of tools in real machining operations are influenced by unmodeled stochastic factors such as inhomogeneities in material quality, chip discontinuity, the workpiece surface, randomness in the cutting resistance, and friction [6, 35], or due to fluctuations during machining. The combined stochastic effect of such unmodeled effects from disparate sources can be incorporated into the governing equations as *noise*. In this context, noise captures random variations in cutting force parameters of the DDE. Noise can alter the dynamics and cause the system to intermittently hop between the underlying deterministic multiple stable states, leading to noise-induced intermittency [36]. This is distinct from other routes to intermittency known in the context of deterministic systems[37]. As notions of stable states, bifurcations and routes to intermittency in the stochastic context are different and such systems require separate analyses [38]. The influence of noise in amplification of machine tool vibrations due to coherence resonance has been studied, along with effects on machine tool dynamics [39]. Stochastic analyses of regenerative turning models [35, 40, 41] highlight how noisy fluctuations alter the stability characteristics of turning processes, while a recent work [42] utilizes power spectral density to approximate the dynamical states in a stochastic turning process. While these works separately focus on the regenerative or frictional effects of the orthogonal cutting processes in varied detail, it is also possible to approximate the dynamics of the cutting tool to a fundamental SDOF model with both effects combined [43]. This is a more realistic scenario of what happens during machining, allowing for investigations into nonlinear stability and improving the accuracy of cutting stability prediction, particularly in low-velocity machining [44].

It is observed that, irrespective of the variety and complexity of investigations present in this field, the combined impact of regenerative and frictional nonlinearities under stochastic fluctuations remains unexplored. This omission is critical, as real machining processes are inherently subject to uncertainties arising from material inhomogeneities, chip discontinuities, and tool-workpiece interactions, all of which can significantly alter system stability. To address this gap, the present study builds upon the model proposed by Yan *et. al* [43] and introduces stochasticity in the DDE model,

including both regenerative and nonsmooth frictional effects. Incorporating noise into cutting force dynamics allows for the representation of realistic operating conditions and subsequent investigation of the influence of such random fluctuations within the multi-stable region, particularly on transitions between coexisting states for the first time.

The rest of this paper is organized as follows. In Section 2, the mathematical formulations of both the deterministic and stochastic DDE models for turning are introduced. Section 3 presents a linear stability analysis and discusses the role of nonsmooth friction in predicting stability. It also provides a nonlinear bifurcation analysis of the deterministic model, identifying three distinct stability regions. In Section 4, stochastic bifurcations, namely, P- and D-bifurcations, are discussed. In Section 5, the stability of the stochastic attractors is studied by computing the basin stability and comparing the values of various entropy measures. Finally, the outcomes of the work are summarized in Section 6.

2 Mathematical Model

The cutting process, illustrated in Fig. 1, refers to the complex dynamical interactions between a machine tool and a workpiece. To systematically analyze the dynamics of the tool, a deterministic model is first introduced, followed by the incorporation of multiplicative stochastic effects to account for unmodeled effects.

2.1 The Deterministic Machining Model

Tool's dynamics in a turning process is modeled as a classical single degree of freedom (SDOF) model with damping c [$N s m^{-1}$], stiffness k [$N m^{-1}$], and mass m [kg] corresponding to the tool [43] as shown in the schematic in Fig. 2. The radius of the workpiece is $R = D/2$ [m] and it has the workpiece speed of $V_c = \frac{2\pi RN}{60}$ [ms^{-1}] where N [$rev min^{-1}$] here represents the spindle speed. During turning, the chip is formed through the process of yielding elasto-plastic deformation when the stationary tool and the rotating workpiece make contact [11].

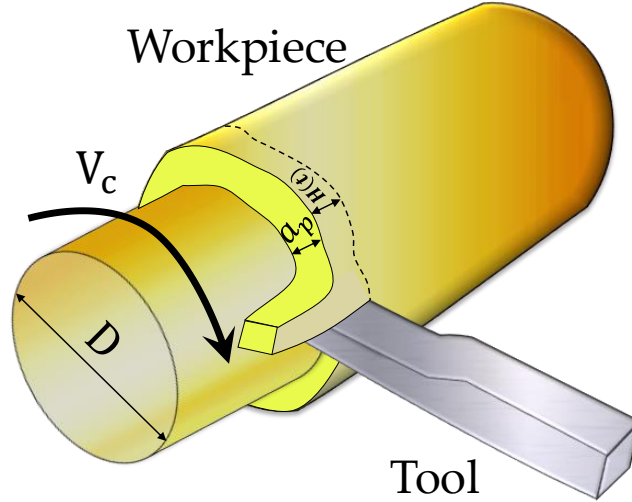


Figure 1: Schematic of the turning process representing the orientation of the tool and workpiece and their relative directions of motion.

During cutting, the material flows along the tool's rake face, which is inclined at an angle γ and oriented perpendicular to the workpiece, with a velocity of V_{ch} [ms^{-1}]. In Fig. 2, the forces F_γ [N] and $F_{\gamma n}$ [N] represent the tangential and normal components generated by the pressing and rubbing of the material against the rake face. The resultant force F_r [N] is then resolved into the cutting force F_c [N] in x -direction and feeding force F_f [N] in y -direction. The interaction between the uncut material and flank face of the tool results in process damping force F_d [N] in the y -direction. The dynamics of the tool shown in Fig. 2 in the vertical direction is governed by the equation

$$m\ddot{Y}(t) + c\dot{Y}(t) + kY(t) = F_f + F_d. \quad (1)$$

The expressions for the forces are given by,

$$F_d = -C_y a_p \frac{\dot{Y}(t)}{V_c}, \quad (2a)$$

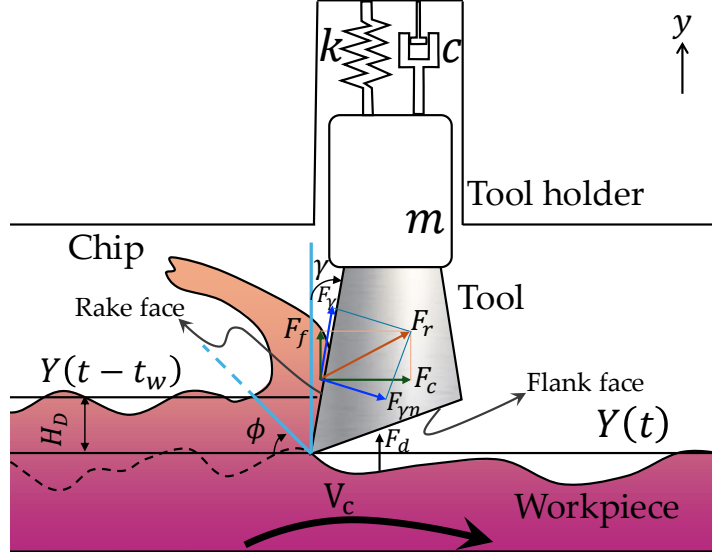


Figure 2: Schematic of the turning process modeled as a spring-mass-damper system representing various cutting forces.

$$F_f = F_\gamma \cos(\gamma) - F_{\gamma n} \sin(\gamma), \quad (2b)$$

where C_y , a_p , and γ denote the process damping coefficient, depth of cut, and rake angle of the tool, respectively. The normal and tangential forces are of the form

$$F_{\gamma n} = K a_p H(t), \quad (3a)$$

$$F_\gamma = \mu F_{\gamma n}, \quad (3b)$$

where $H(t)$ denotes the instantaneous thickness of the chip and has the form

$$H(t) = H_D - Y(t) + Y(t - t_w). \quad (4)$$

Here H_D [m] and $t_w = \frac{60}{N}$ represent the nominal thickness of the chip (feed rate) and the rotational period of the workpiece, respectively. K and a_p in Eq. (3) represent the cutting force coefficient and depth of cut, respectively. The term μ is the equivalent frictional coefficient corresponding to the Stribeck frictional model [14]

$$\mu = \text{sign}(V_\gamma) \left(\mu_d + (\mu_d - \mu_s) \exp\left(-\frac{|V_\gamma|}{V_s}\right) \right), \quad (5)$$

where V_s [$m s^{-1}$] is the Stribeck velocity, μ_s , and μ_d are the static and dynamic friction coefficients respectively. V_γ [$m s^{-1}$] represents the frictional velocity of the chip relative to the tool in the form

$$V_\gamma = V_{ch} - \dot{Y}(t) \cos(\gamma), \quad (6)$$

where $V_{ch} = V_c \frac{\sin(\phi)}{\cos(\phi - \gamma)}$ [$m s^{-1}$] denotes the chip velocity and ϕ denotes the shear angle of the cutting tool. Fig. 3 illustrates the classical Stribeck friction law employed in the turning model. The friction coefficient exhibits characteristic stick-slip behavior, rapidly decaying from the static value μ_s at low velocities to the dynamic value μ_d for $|V_\gamma| \gg V_s$. The turning model described in Eq. 1 can be nondimensionalized as

$$\xi = \frac{c}{\sqrt{mk}}, v_s = \frac{30V_s \cos(\gamma - \phi)}{\pi R \sin(\phi)} \sqrt{\frac{m}{k}}, c_y = \frac{30C_y}{\pi R K}, v = \frac{H_D}{V_s} \sqrt{\frac{k}{m}}, n = N \sqrt{\frac{m}{k}}, \tau_w = \frac{60}{n} = t_w \sqrt{\frac{k}{m}}, \Omega = \frac{2\pi}{\tau_w},$$

and

$$W = a_p \frac{K}{k}, \quad (7a)$$

$$\tau = t \sqrt{\frac{k}{m}}, \quad (7b)$$

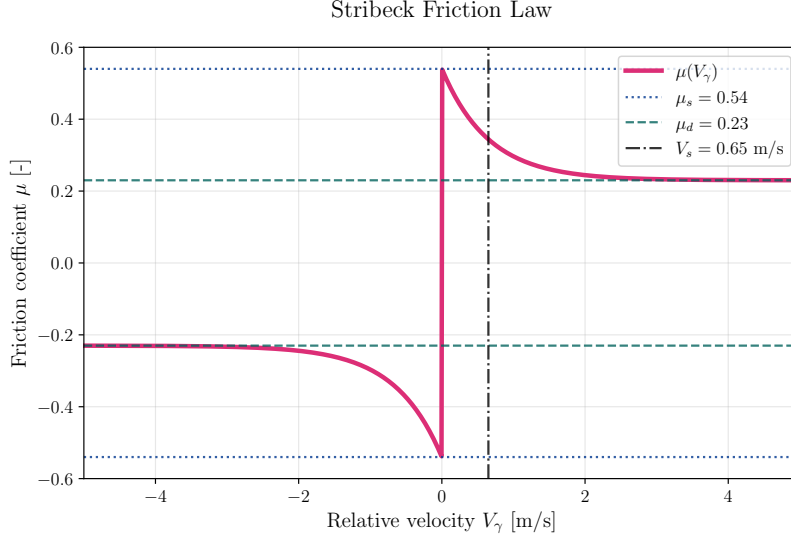


Figure 3: Stribeck friction coefficient $\mu(V_\gamma)$ with parameters $\mu_d = 0.23$, $\mu_s = 0.54$, $V_s = 0.65 \text{ ms}^{-1}$. The antisymmetric curve shows an exponential transition from static to dynamic friction regimes around the Stribeck velocity.

$$y_1(\tau) = \frac{Y(t)}{H_D}, \quad (7c)$$

$$y_2(\tau) = \dot{y}_1(\tau) = \frac{\dot{Y}(t)}{H_D} \sqrt{\frac{m}{k}}, \quad (7d)$$

$$v_\gamma = \frac{V_\gamma}{H_D} \sqrt{\frac{m}{k}} = \frac{n}{v_s} - v \cos(\gamma) y_2(\tau). \quad (7e)$$

The non-dimensional equation of the model is obtained as follows:

$$\ddot{y}(\tau) + \xi \dot{y}(\tau) + y(\tau) = f_f + f_d, \quad (8a)$$

with

$$f_f = W(\mu_{vs} \cos(\gamma) - \sin(\gamma)) h(\tau), \quad (8b)$$

$$f_d = -W c_y \frac{\dot{y}}{n}, \quad (8c)$$

$$\mu_{vs} = \text{sign}(g) \left(\mu_d + (\mu_s - \mu_d) e^{|-g|} \right), \quad (8d)$$

$$\text{where } g = \frac{n}{v_s(\gamma, \phi)} - v \cos(\gamma) \dot{y}(\tau), \quad (8e)$$

$$\text{and } h(\tau) = 1 - y(\tau) + y(\tau - \tau_w). \quad (8f)$$

2.2 The Stochastic Dimensionless Equation for Turning

Turning involves complex interactions and unpredictable factors, making it a highly nonlinear and stochastic process. This is reflected in both qualitative and quantitative behaviors observed in deterministic numerical models that simulate such processes [12, 17, 31, 43]. The introduction of stochastic effects further modifies these dynamic behaviors. Here, a noise term is introduced to the expressions of the depth of cut in the cutting forces (8b) and (8c) to study the combined effects of these complex processes. The resulting equation now accommodates unmodeled effects such as workpiece material inhomogeneities, surface roughness on the workpiece or tool wear, built-up edge over the rake and flank faces, or environmental disturbances. The resulting non-dimensional stochastic DDE is

$$\ddot{y}(\tau) + \xi \dot{y}(\tau) + y(\tau) = \bar{f}_f + \bar{f}_d, \quad (9)$$

with

$$\bar{f}_f = W(1 + \eta\lambda(\tau))(\mu_{vs} \cos \gamma - \sin \gamma)h(\tau), \quad (10a)$$

$$\bar{f}_d = -W(1 + \eta\lambda(\tau))\frac{K}{k}c_y\frac{\dot{y}}{n}, \quad (10b)$$

where η is the intensity of the noise and $\lambda(\tau)$ is modeled as an Ornstein-Uhlenbeck process, governed by

$$d\lambda(\tau) = \theta\{\mu_{OU} - \lambda(\tau)\}d\tau + \sigma dW(\tau), \quad (11)$$

where μ_{OU} is the process mean, σ is the volatility, θ denotes the mean reversion speed and $dW(\tau)$ are the increments of a Wiener process. An Ornstein-Uhlenbeck process is chosen to model the fluctuating term in the system since it is a stationary Gaussian Markov process with zero mean. This process has been used in several studies to model regenerative chatter in metal cutting where delay and stochastic effects interact across multiple time scales [45], investigate stochastic P-bifurcations in nonlinear impact oscillators with soft barriers [46], and analyze vibro-impact systems driven by noise [47].

3 Deterministic Analysis

3.1 Linear stability analysis

In steady state cutting, the tool's dissipative and elastic responses equilibrate the cutting forces. Under these steady-state conditions, the tool's static deformation is determined by solving the equilibrium form of Eq. (8a). This equation can be rewritten as

$$y_1(\tau) = y_2(\tau), \quad (12a)$$

$$\dot{y}_2(\tau) = -y_1(\tau) - \xi y_2(\tau) + W[\mu_{vs} \cos(\gamma) - \sin(\gamma)]h(\tau) - Wc_y\frac{y_2(\tau)}{n}. \quad (12b)$$

For steady state, with no vibration, the tool displacement is constant, velocity is zero and there will be no regeneration effect ($y_1(\tau) = y_1(\tau - \tau_w) = y_{10}$)

$$\therefore (y_1(\tau), y_2(\tau)) \equiv (y_{10}, 0), \quad (13)$$

where

$$y_{10} = W \left[\mu_d + (\mu_s - \mu_d) \exp\left(-\frac{n}{v_s}\right) \right] \cos(\gamma) - W \sin(\gamma). \quad (14)$$

A perturbation of the stationary cutting process causes the tool to oscillate around the equilibrium point given in Eq. (14). The local stability of $(y_{10}, 0)$ is then evaluated by linearizing Eq. (12), which yields

$$\dot{\mathbf{y}}(\tau) = \mathbf{A}\mathbf{y}(\tau) + \mathbf{D}\mathbf{y}(\tau - \tau_w), \quad (15)$$

where

$$\mathbf{y} = \begin{pmatrix} y_1 \\ y_2 \end{pmatrix}, \mathbf{A} = \begin{pmatrix} 0 & 1 \\ -(1 + Wa) & -(\xi + Wb) \end{pmatrix}, \mathbf{D} = \begin{pmatrix} 0 & 0 \\ Wa & 0 \end{pmatrix} \quad (16)$$

The coefficients a and b in Eq. (16) as follows

$$a = \left(\mu_d + (\mu_s - \mu_d) \exp\left(-\frac{n}{v_s}\right) \right) \cos(\gamma) - \sin(\gamma), \quad (17a)$$

$$b = \frac{c_y}{n} + (\mu_d - \mu_s)\gamma \cos^2(\gamma) \exp\left(-\frac{n}{v_s}\right). \quad (17b)$$

The stability is then determined by the eigenvalues of the following characteristic equation.

$$\det(\lambda \mathbf{I} - \mathbf{A} - \mathbf{D}e^{-\lambda \tau_w}) = 0, \quad (18)$$

where $\det(\bullet)$ represents a determinant and λ denotes the eigenvalues. For the equilibrium to remain stable, all eigenvalues of the linearized system must lie strictly in the left half of the complex plane, meaning each has a negative real part. If, however, even a single eigenvalue acquires a positive real part, the perturbation grows instead of diminishing, and the stationary cutting becomes unstable. At the boundary between these two regimes, the point of critical stability is where the system exhibits a pair of purely imaginary eigenvalues, $\lambda = \pm i\omega$. This pair signals the onset of self-excited oscillations, as the system transitions from decaying motion to sustained vibration [48]. Substituting this critical condition into Eq.(18) transforms the characteristic equation

$$\det(i\omega \mathbf{I} - \mathbf{A} - \mathbf{D}e^{-i\omega \tau_w}) = 0, \quad (19)$$

or

$$\omega^2 - 1 - Wa[1 - \cos(\omega\tau_w)] = 0, \quad (20a)$$

$$\omega(\xi + Wb) + Wa\sin(\omega\tau_w) = 0. \quad (20b)$$

The detailed derivation of Eq. (20) is provided in Appendix A. As indicated in Eq. (17), both a and b depend on non-dimensionalised spindle speed $n = \frac{\tau_w}{60}$, which renders Eq. (20) transcendental and prevents a closed-form analytical solution. Therefore, the stability lobes are computed via a numerical eigenvalue analysis using the Newton-Raphson continuation scheme. The complete continuation algorithm is provided in Appendix B. All numerical hyperparameters used in the predictor–corrector scheme are summarized here for clarity. The initial predictor step (inc) used to generate the second point is set to 2×10^{-5} . The continuation ratio (rat), which controls the predictor step scaling, is set to 1.005. Each curve is allowed to grow to a maximum of $\max C = 1000$ points, while the number of attempts to locate a valid second point is limited to $\max T = 30$. The nonlinear solver accepts a solution only when the residual norm satisfies $\|F\|_{\text{tol}} = 10^{-10}$, and duplicate seed points are removed using a strict tolerance of $\text{dup}_{\text{tol}} = 10^{-12}$. Finally, the fixed parameter W^* is selected such that the resulting a_p slightly exceeds the region of interest (in this study, 2 mm).

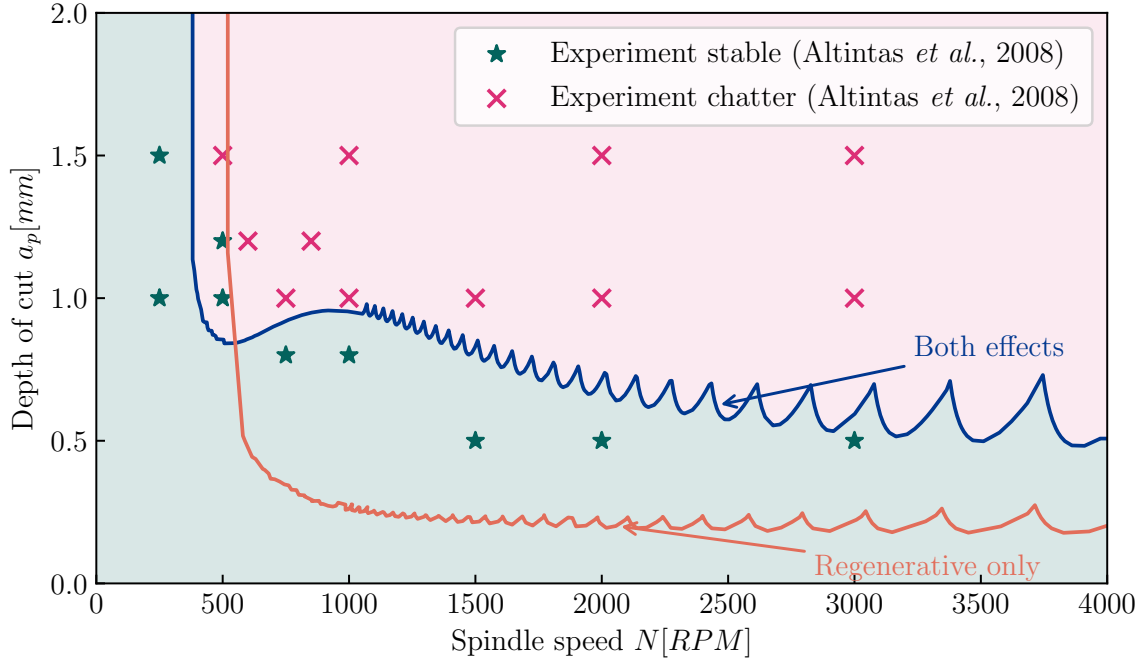


Figure 4: The stability lobe diagram shows the numerically computed stable region in green and the chatter region in magenta. The blue curve depicts the stability lobes for the model with both frictional and regenerative effects, whereas the orange curve shows the lobes for the regenerative and static-friction model. The red crosses denote chatter and the green stars indicate stable cutting as observed experimentally by Altintas *et al.*[49].

For this entire paper, the parameter values are adopted from [44], with $m = 0.561$ [kg], $c = 145$ [Nsm⁻¹], $k = 6.48 \times 10^6$ [Nm⁻¹], $K = 6.02 \times 10^9$ [Nm⁻²], $C_y = 6.11 \times 10^5$ [Nm⁻¹], $R = 0.0175$ [m], $H_D = 0.0005$ [m], $\gamma = 0^\circ$, $\phi = 45^\circ$, $V_s = 0.65$ [ms⁻¹], $\mu_d = 0.23$, $\mu_s = 0.54$. These values yield the following dimensionless parameters: $\xi = 0.07605$, $\nu_s = 0.10436$, $\nu = 2.61434$, and $c_y = 0.05541$. By substituting these parameter values into Eq. (20), the corresponding stability boundaries are computed. Fig. 4 illustrates the stability lobe diagram obtained from the numerical eigenvalue analysis. In Fig. 4, the blue line indicates the stability boundary computed from solving the critical equations (20) of the model, which has both the regenerative and frictional effects. This line separates the space into two regions: the region below the curve is stable (shaded green), and the region above the curve is unstable (shaded magenta). The orange line denotes the stability lobes of the model in the absence of nonsmooth friction. In other words, the friction coefficient is taken as the static friction $\mu_{vs} = \mu_s$. This assumption shifts the stability boundary and the stable cutting data from experiments lie under the unstable region. Therefore, it is important to account for nonsmooth friction in the model to more accurately capture the system dynamics.

3.2 Nonlinear bifurcation analysis

Bifurcation analysis of the DDE model 8a is carried out by considering depth of cut a_p [mm] as the bifurcation parameter for a fixed spindle speed of $N = 3600$ [rev min⁻¹]. The DDE (8a) is numerically solved using MATLAB's *dde23* [50] solver with the step size of $\Delta\tau = 0.01$ for the initial deterministic study. The solver's tolerance settings are set to their default configuration: a relative tolerance (*RelTol*) of 10^{-3} and an absolute tolerance (*AbsTol*) of 10^{-6} . For each value of the bifurcation parameter, the history function is initialized with the solution from the previous parameter value in both forward and backward simulations. All simulations were performed using the non-dimensionalized form of the governing equations. However, for ease of physical interpretation, the results are reconstructed and presented in terms of dimensional quantities, specifically time, instantaneous chip thickness, and frictional chip velocity relative to the tool by applying Eq. (7).

Fig. 5 shows the result of the bifurcation analysis where the maximum and minimum values of the instantaneous chip thickness $H(t)$ and the frictional chip velocity relative to the tool V_γ in dimensional form are plotted along the y -axis while the depth of cut a_p is in the x -direction. The bifurcation analysis reveals that the system's stability is divided into three distinct regions, as listed in Table 1.

Region	Attractor
Non-chatter	Fixed Point
Chatter	Sticking limit cycle
Multi-stable	Fixed Point and sticking limit cycle

Table 1: List of regions with distinct phenomena and corresponding attractors in the dynamical systems sense.

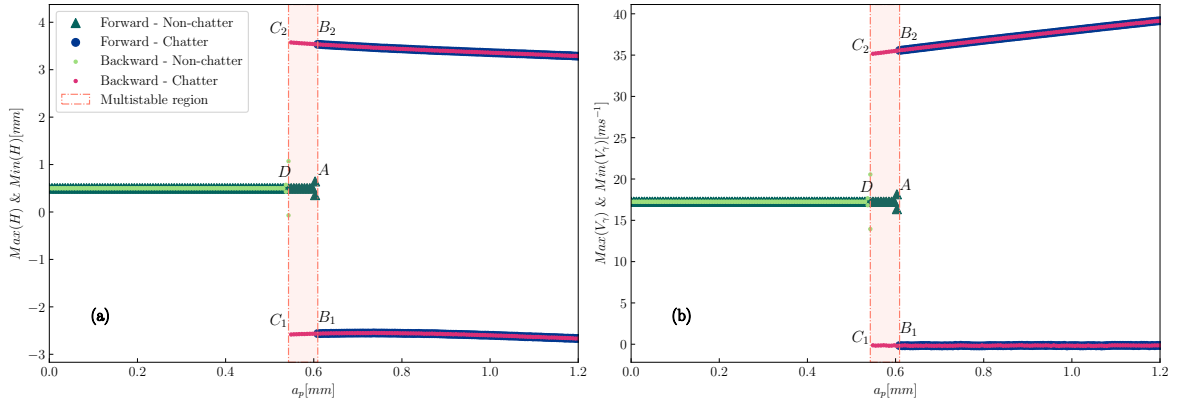


Figure 5: Bifurcation diagram using depth of cut a_p as the bifurcation parameter. Figure (a) shows the maximum and minimum values of chip thickness H , and (b) shows the corresponding maximum and minimum values of frictional velocity V_γ .

The shaded region in Fig. 5 corresponds to the multi-stable region. The dynamical states to the left and right of the multi-stable region represent non-chatter and chatter regions, respectively. It can be observed that in the non-chatter region, the maximum and minimum values of $H(t)$ are the same, whereas in the chatter region, their magnitudes are different, indicating high-amplitude vibrations. Also, in the chatter region, the minimum values of $H(t)$ become negative, indicating loss of contact between the tool and the workpiece. This behavior typically arises from regenerative chatter, in which low spots created during the previous cutting pass influence the tool's engagement in the subsequent pass. The model captures this by dynamically updating the chip thickness $H(t)$ via a delay term that reflects the influence of past position on the tool's current position. This can also be observed from the Figs. 6 (a-b). The chip thickness variation over time is given in Fig. 6 (a) for $a_p = 0.4$ mm and in Fig. 6 (b) for $a_p = 0.8$ mm. From Fig. 6 (a), it is observed that the chip thickness is constant after the transient, which makes the maximum and minimum values have the same value for $a_p = 0.4$ mm in Fig. 5. Similarly, Fig. 6 (b) shows the large amplitude vibrations which reflect two different magnitudes for maximum and minimum values for $a_p = 0.8$ mm in Fig. 5. The phase portrait plotted between dynamic chip thickness and chip velocity for the chatter case is shown in Fig. 6 (c). From Figs. 6 (c) and 5 (b), one can also observe that the minimum value of frictional chip velocity relative to the tool V_γ is zero during chatter cutting dynamics. This happens in an orthogonal cutting with a stationary cutting tool, when the chip velocity V_{ch} matches the velocity of the tool surface at the rake face, where the rake face doesn't move. This alters the normal cutting mechanics,

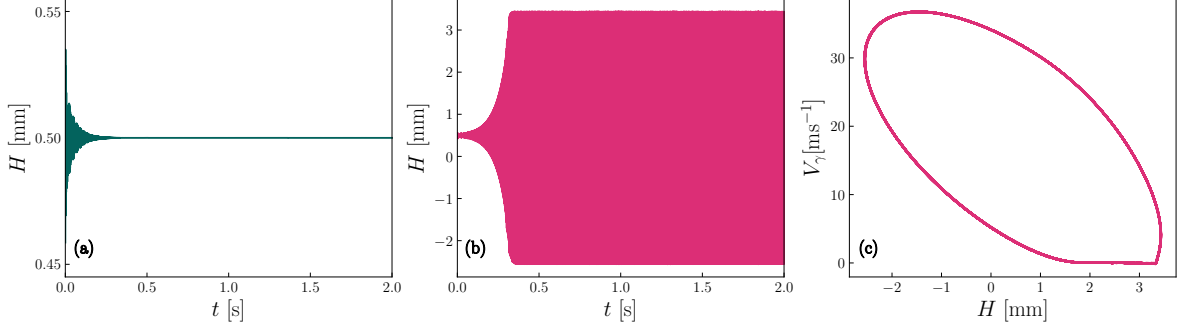


Figure 6: (a) Variation of chip thickness over time for the stable case $a_p = 0.4 \text{ mm}$, (b) Variation of chip thickness over time for the unstable case $a_p = 0.8 \text{ mm}$, and (c) Phase portrait of an unstable cutting showing the sticking dynamics of the tool.

leading to chatter. The DDE 8a is integrated up to a dimensionless time of $\tau = 4.5 \times 10^3$, with the resulting dynamics subsequently represented in terms of the physical time variable t . Also, from Fig. 5 it is noticed that the cutting stability switches from point A to points B_1 and B_2 during the forward simulation, corresponding to an increase in the depth of cut a_p from 0.2 mm to 1.2 mm . However, the results of backward simulation show that the stability jumps from points C_1 and C_2 to D , resulting in a multi-stable region at certain values of the bifurcation parameter. In this region, the system's stability depends significantly on the tool condition, the initial profile of the workpiece surface, and stochastic fluctuations, which account for various unmodeled effects. While the first two factors can typically be estimated and controlled before the cutting process begins, realistic scenarios across diverse application sectors underscore the critical need to understand system dynamics under noisy conditions. Incorporating noise into the numerical analysis is thus essential for clearly demarcating chatter occurrence, controlling chatter, and ensuring stable cutting throughout the cutting process.

4 Stochastic Analysis

In deterministic systems, bifurcation analysis involves examining the system's long-term behavior as parameters vary. However, stochastic systems are continuously influenced by external fluctuations, which prevent the dynamics from settling on the underlying deterministic attractors. In addition, there is always a non-zero probability of noise dislodging the dynamics from the vicinity of an attractor. As a result, the conventional definition of bifurcation used in deterministic settings must be adapted to account for these fluctuations when conducting stability analysis in stochastic systems. For a stochastic process given in Equation 21

$$d\mathbf{X}_t = \mathbf{f}(t, \mathbf{X}_t)dt + \sigma_g \mathbf{g}(t, \mathbf{X}_t)d\mathbf{W}_t, \quad \mathbf{X}_t \in \mathbb{R}^n, \quad (21)$$

where $\mathbf{f}(t, \mathbf{X}_t)$ represents the deterministic component governing the system's dynamics, also known as the drift term, $\mathbf{g}(t, \mathbf{X}_t)$ represents the diffusion terms, governing the magnitude of stochastic fluctuations in the dynamical system, σ_g is the noise intensity and $d\mathbf{W}_t$ is the Wiener process increment. For stochastic analysis, the stochastic DDE (9) was solved using the Euler-Maruyama [51] scheme in MATLAB.

The numerical solutions obtained with different step sizes $\Delta\tau$ from 10^{-1} to 10^{-5} validated against the solution at a very fine step size of ($\Delta\tau = 10^{-6}$), as illustrated in Fig. 7. Analyzing peak-to-peak values of $y(\tau)$ reveals the magnitude of the optimal step size to be at $\Delta\tau = 10^{-3}$ with only 1.0% relative amplitude error. This represents a substantial improvement over the coarser steps (2.3% at $\Delta\tau = 10^{-2}$, 5.3% at $\Delta\tau = 10^{-1}$) and thus was selected for further stochastic analysis simulations to ensure computational efficiency. The history function for this case is considered in the form of a Fourier expansion of multiple harmonics. More details regarding the history function and its relation with the initial configuration are given in section 5.1.

A stochastic attractor can be defined as a set $A \subset \mathbb{R}^n$ such that once the system is in the bounded region A , it remains in A for a finite time t under consideration despite the influence of stochastic fluctuations. For any initial state \mathbf{X}_0 in the basin of the attractor, $P(\mathbf{X}_t \in A) \rightarrow 1$ as $t \rightarrow \infty$ [52]. The systems with stochastic excitations have been studied under the purview of two distinct classes of bifurcations, namely, P-bifurcation and D-bifurcation[36, 38, 52].

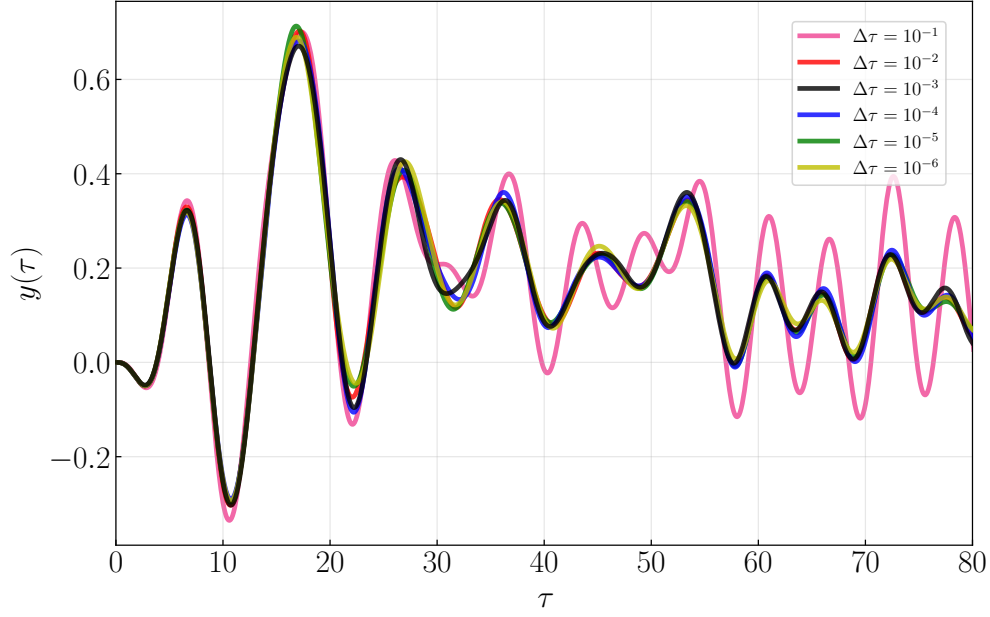


Figure 7: Comparison of numerical solution obtained with different time steps using the Euler-Maruyama scheme for the stochastic case. Pink, red, black, blue, green, and yellow color lines represent the numerical solution with time steps 10^{-1} , 10^{-2} , 10^{-3} , 10^{-4} , 10^{-5} and 10^{-6} , respectively.

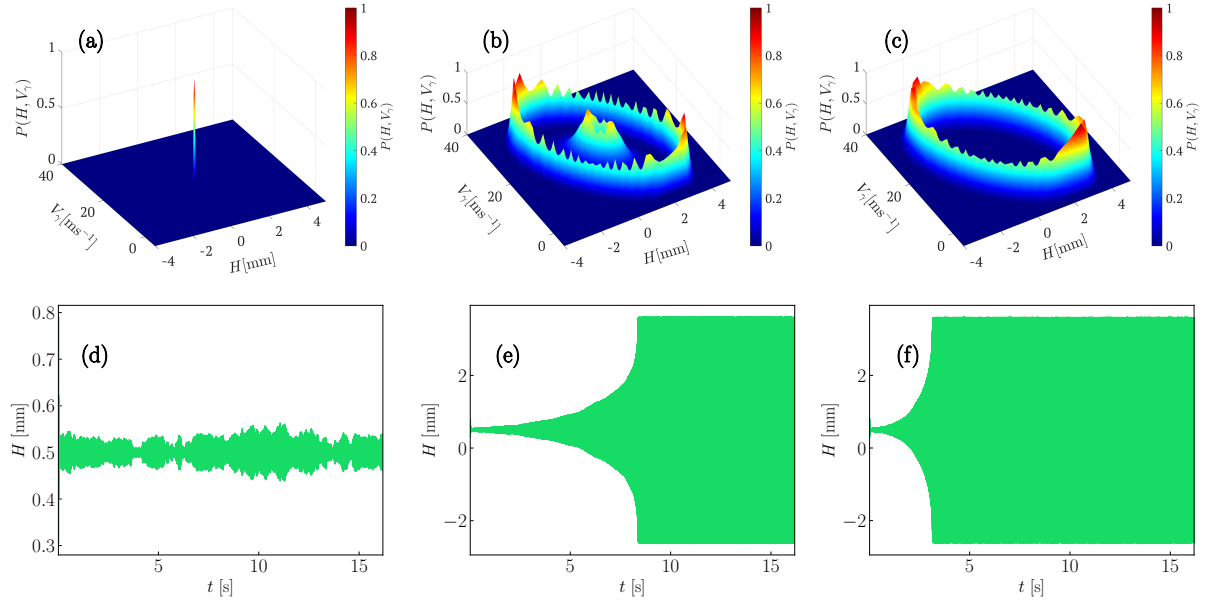


Figure 8: Stochastic P-bifurcation of the metal cutting system for the parameter values of $\eta = 0.15$, $\mu_{OU} = 0.1$, $\sigma = 0.2$, $\theta = 0.7$. Figures (a)-(c) show the probability density values for depth of cut values of $a_p = 0.52$ mm, 0.54 mm, 0.55 mm. (d)-(f) show the corresponding chip thickness over time.

4.0.1 P-bifurcation

Phenomenological or *P-bifurcations* arise when changes in a system parameter cause abrupt topological shifts in the probability distribution governing its long-term behaviour [36, 38]. The joint probability density (*j-pdf*) represents a statistical measure of how much time a typical system trajectory spends within a given volume element in the phase space. It also indicates the spatial extent of a stochastic attractor [36]. Fig. 8 depicts the occurrence of the *P-bifurcation* in the considered system where the stochastic parameters are taken as $\eta = 0.15, \mu_{OU} = 0.1, \sigma = 0.2, \theta = 0.7$. Figs. 8 (a)-(c) correspond to the *j-pdf* for three different bifurcation parameter values $a_p = 0.52 \text{ mm}, a_p = 0.54 \text{ mm}$ and $a_p = 0.55 \text{ mm}$ respectively. It can be observed that there is a peak in Fig. 8 (a), which indicates the fixed point attractor. Fig. 8 (b) shows a crater-like shape with a peak inside, indicating the occurrence of a transition of the dynamical state from one underlying deterministic attractor to another. The stability of the system switches from the non-chatter to the chatter region under the influence of noise. Further, the inside peak disappears in Fig. 8 (c) with the further increase of a_p . The corresponding changes in the dynamics are shown in Figs. 8 (d)-(f), which present the instantaneous chip thickness. In particular, it is evident from Fig. 8 (e) that the attractors corresponding to both the non-chatter and the chatter cutting appear to have non-zero probabilities of occurrence when the dynamics is observed for a sufficiently long time. In this analysis, time histories were simulated under the assumption of ergodicity. This assumption implies that time-averaged statistics obtained from a single, sufficiently long trajectory are equivalent to ensemble-averaged quantities across multiple realizations [38]. The simulations are carried out for $\tau = 5.5 \times 10^4$. The *j-pdf* values are numerically computed using the kernel smoothing function estimate *ksdensity* in MATLAB. To visualize the P-bifurcation quantitatively, the area of the contours of the *j-pdf* at a specific value of probability $P = 0.5$ is computed using a MATLAB routine *Contour2Area* [53] and the results are shown in Fig.9. In this calculation, the values of a_p are set to 0.5-1.2 mm with a step size of 0.005. Fig. 9 (d) displays the normalized area corresponding to contour levels at a *j-pdf* value of 0.5. Sub-figures (a)-(c) and (e)-(g) illustrate how the contour shapes (*j-pdf*=0.5) evolve across various values of a_p , specifically, (a) 0.5 mm, (b) 0.54 mm, (c) 0.55 mm, (e) 0.595 mm, (f) 0.8 mm, and (g) 1.2 mm. The morphological changes observed in these contours are reflected quantitatively in the area trend shown in Fig. 9 (d). It is observed that there is a sudden jump in the area exactly at the beginning of the multi-stable region $a_p = 0.54 \text{ mm}$, which coincides with the topological changes shown in Fig. 8, indicating that a P-bifurcation has taken place.

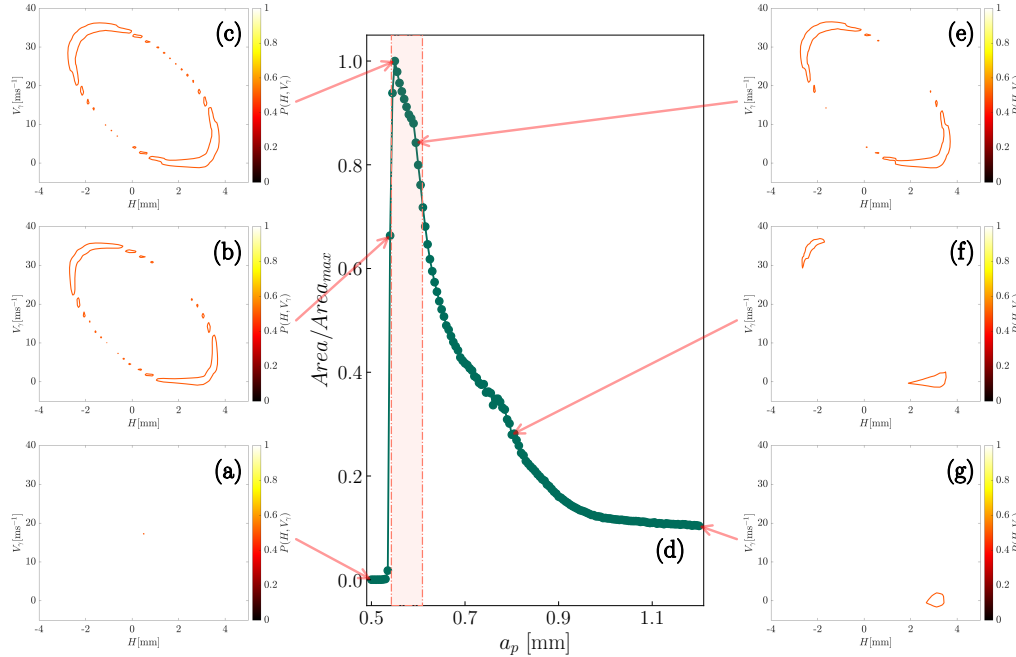


Figure 9: Figure (d) representing the area of the contours at $j\text{-pdf} = 0.5$. The shaded region denotes the multi-stable region. The left and right panels show the contour plots of probability equal to 0.5 for specific depth of cut (a_p) values, namely, (a) 0.5, (b) 0.54, (c) 0.55, (e) 0.595, (f) 0.8, and (g) 1.2 mm.

4.0.2 D-bifurcation

Dynamical or *D-bifurcations* refer to sudden topological changes in the underlying phase-space dynamics [36]. Unlike *P-bifurcations*, which characterize qualitative changes in the shape of *j-pdf*, *D-bifurcations* reflect shifts in the dynamical stability of stochastic attractors. Stability is assessed by calculating Lyapunov exponents (LE), which quantify the average exponential rate of divergence or convergence of nearby trajectories. In stochastic systems with continuous perturbations, a negative LE indicates that perturbations remain bounded and the system tends toward a stochastic attractor, even though individual fluctuations persist due to the added noise. For the *D-bifurcation* analysis following approximation for LE has been used [54].

$$\Lambda = \lim_{\tau \rightarrow \infty} \lim_{\delta \rightarrow 0} \mathbb{E} \left(\frac{1}{\tau} \log \left(\frac{|y(\tau) - y_{pert}(\tau)|^2}{\delta} \right) \right), \quad (22)$$

where $y_{pert}(\tau)$ is the perturbed trajectory with small perturbation δ with respect to the original trajectory $y(\tau)$ and \mathbb{E} denotes the expectation operator. Fig. 10 visualizes the LE values Λ as a function of the depth of cut a_p . From

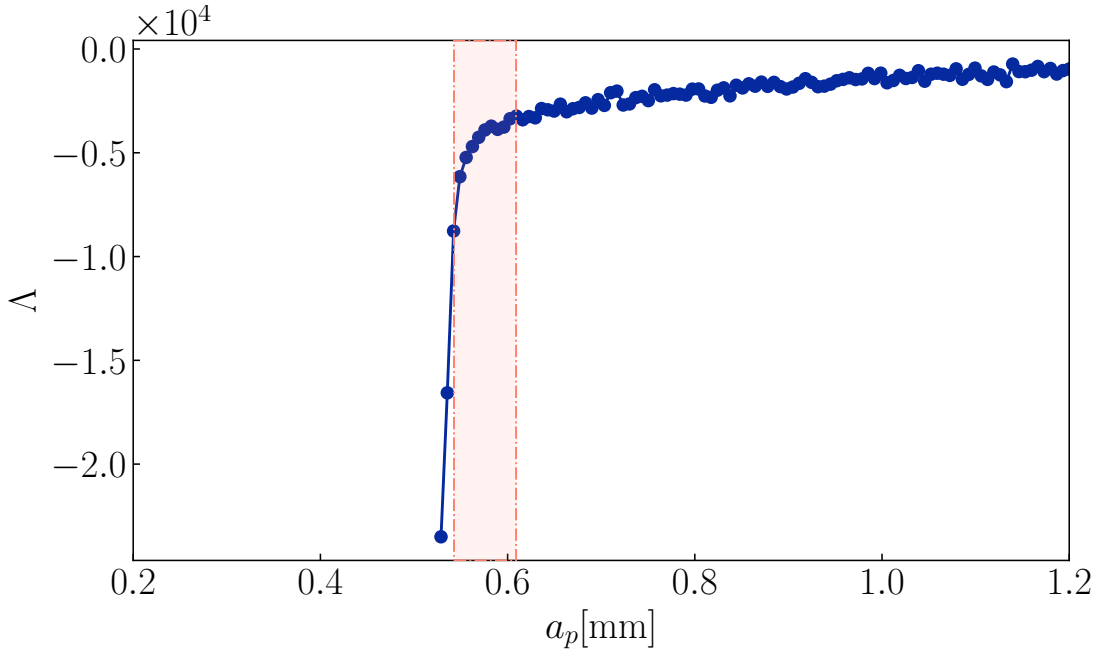


Figure 10: Estimation of Lyapunov exponent with a_p as the bifurcation parameter.

Fig. 10, one can observe that LE has negative values over all the values of a_p . This is due to the stable nature of both attractors. However, there are no data points in Fig. 10 for a_p ranging from 0.2 to 0.53 mm, as the corresponding LE values approached $-\infty$, indicating that the perturbations were too small to produce divergence. The first point in Fig. 10 is around $a_p = 0.53$ mm where the transition in the dynamics occurred and has a gradually increasing trend at the start of the multi-stable region and settled around -1.2×10^4 . The *D-bifurcation* occurs at $a_p = 0.53$ mm, whereas from Fig. 8 (b) it is evident that the peak structure still exists inside the crater-like structure and it disappears at $a_p = 0.55$ mm. It is important to mention here that the *D-bifurcation* occurs at a different value of the bifurcation parameter than the *P-bifurcation*[36].

5 Stability of stochastic attractors

In the previous section, the computations were performed under the assumption that, for a given bifurcation parameter, the initial history function remained identical across all trials. However, experimental studies show that the initial surface profiles of the workpiece have a significant effect on the stability of the dynamics of cutting tools [55]. This necessitates studying uncertainty in initial surface profiles, which is done using the method of basin stability analysis. Monte Carlo simulations have been carried out with continuously present perturbations and variations in initial history functions. The

regimes to be operated into avoiding chatter, particularly in the multi-stable region, have been demarcated. Furthermore, entropy metrics are carried out to characterize transitions in system dynamics by analyzing the statistical structure of the underlying time histories.

5.1 Basin stability analysis

Basin stability for a system without delay is normally computed by considering the percentage of initial conditions settling into each attractor in the dynamical system[56]. However, calculating basins of attraction in the same manner for a DDE needs reconsideration, as such systems have infinite initial conditions. The computation of basin stability analysis for the stochastic case is adapted from the deterministic basin stability computation as given in Refs . [44, 48]. The expressions for the initial history function are considered as

$$y_1(\tau) = s(\theta_{bs}(\tau)) - p_u(\theta_{bs}(\tau)), \quad (23a)$$

where

$$p_u(\theta_{bs}(\tau)) = 1 - \frac{\theta_{bs}(\tau)}{2\pi}, \quad (23b)$$

$$\theta_{bs}(\tau) = 2\pi + \tau\Omega, \quad \tau \in [-\tau_w, 0), \quad (23c)$$

and the $s(\theta_{bs}(\tau))$ represented by the following Fourier series

$$\begin{aligned} s(\theta_{bs}(\tau)) = & \sum_{i=1}^{N_{bs}} a_i (\sin(i\Omega\tau + i\phi_{bs}) - \sin(i\phi_{bs})) \\ & + \sum_{i=1}^{N_{bs}} b_i (\cos(i\Omega\tau + i\phi_{bs}) - \cos(i\phi_{bs})), \end{aligned} \quad (23d)$$

where the coefficients a_i and b_i specify the initial waviness length and height of the workpiece surface. Fig. 11 shows

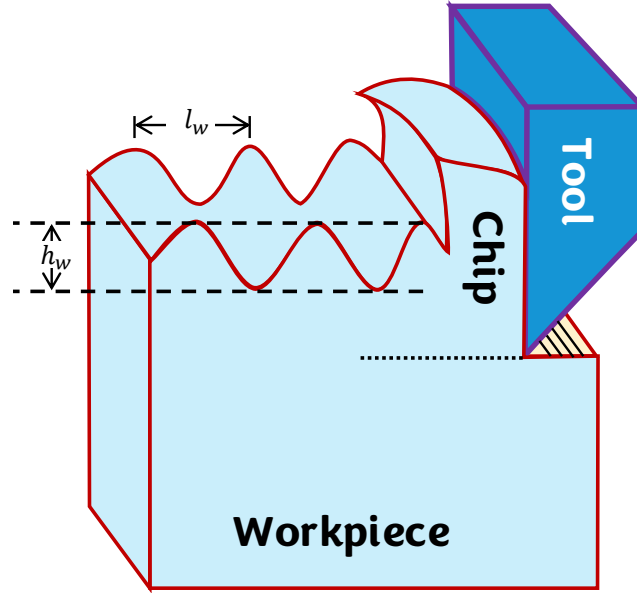


Figure 11: Schematic figure showing initial waviness and height

the schematic diagram of waviness height (h_w) and length (l_w). $\phi_{bs} \in [0, 2\pi)$ represents the tool-workpiece engagement geometry at the onset of cutting. To set the limits on waviness length and height, the following constraint was used in the initial function when calculating basin stability.

$$\sum_{i=1}^{N_{bs}} a_i^2 + b_i^2 \leq \alpha^2. \quad (24)$$

Also, to restrict the strength of initial tool vibrations, another constraint is considered as follows

$$y_1(0) \in [-\beta, \beta], \quad (25a)$$

$$y_2(0) \in [-\beta, \beta]. \quad (25b)$$

The basin stability in the multi-stable region can be computed by considering the initial history function (23), based on Monte-Carlo simulations with M_{bs} groups of coefficients, $\{a_1^{(j)}, \dots, a_n^{(j)}, b_1^{(j)}, \dots, b_n^{(j)}, y_1(0)^{(j)}, y_2(0)^{(j)}, \phi_{bs}^{(j)}\}_{j=1}^{M_{bs}}$. The stochastic version of the considered model (9) is solved using the initial function (23) approximation for the following parameter values: stochastic process parameters $\eta = 0.15$, $\mu_{OU} = 0.1$, $\sigma = 0.2$, $\theta = 0.7$, the system parameters $a_p = 0.54 \text{ mm}$, $N = 3600 \text{ RPM}$, and the constraints are fixed as $\alpha = \beta = 6$. In this study, a total of $M_{bs} = 1000$ Monte Carlo simulations were performed, each run over a non-dimensional time (τ) of 1.1×10^4 . Fig. 12 shows the number of samples leading to the sticking limit cycle attractor M_{CH} as a function of the number of basis functions N_{bs} . It is clear

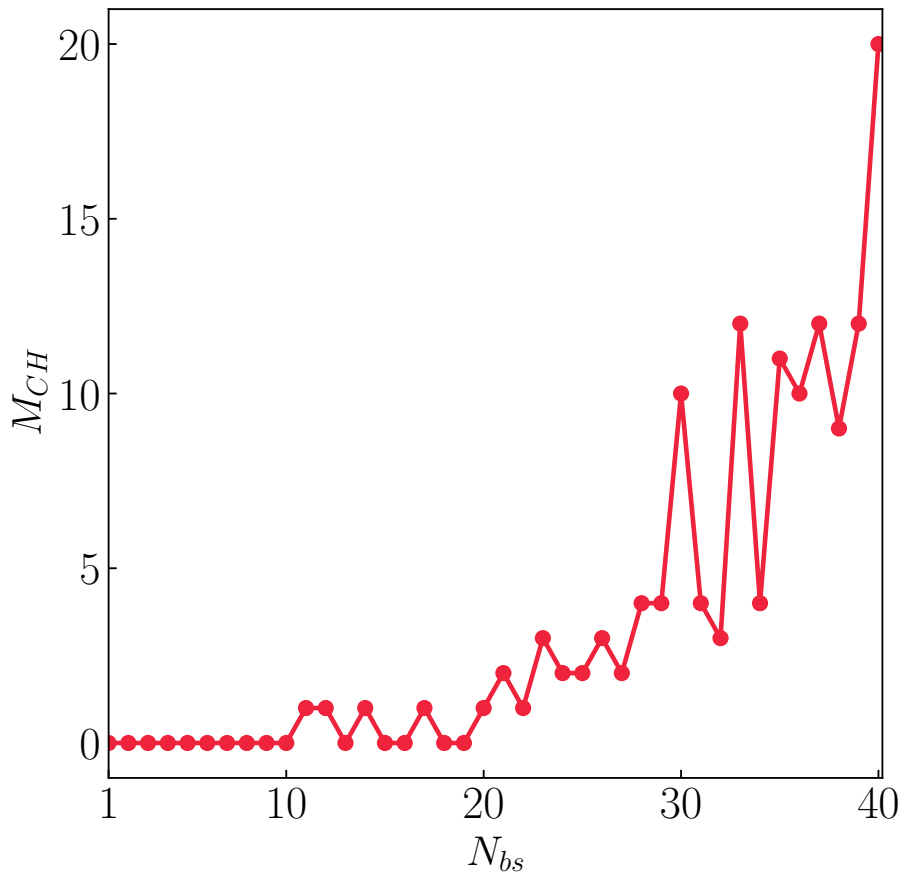


Figure 12: Basin stability of chatter cutting is estimated and displayed as functions of the number of basis functions N_{bs} . The constraint parameters are $\alpha = \beta = 6$. The y-axis shows the number of samples that lead to chatter cutting.

that increasing the number of basis functions, N_{bs} , results in a more uneven workpiece surface, which, in turn, affects the tool's stability. When N_{bs} exceeds 20, M_{CH} begins to increase, reaching its maximum value of 20 at $N_{bs} = 40$. A higher initial surface roughness, with $M_{CH} \geq 10$, holds a non-zero probability of driving the system to a state of chatter under noisy fluctuations. The same analysis has been carried out by tweaking the constraint parameters, depicting varied heights and widths of irregularities in the workpiece, initial tool displacement, and the results are plotted in $\{\alpha, \beta\}$ space for various values of N_{bs} in Fig. 13. The first heat-map sub-figure 13 (a) corresponds to $N_{bs} = 8$, and it shows no variation in the color, indicating that all the 1000 samples lead to the non-chatter fixed point attractor. In other words, if the initial roughness of the workpiece is low or moderate, then the probability of noisy fluctuations pushing the dynamics to the vicinity of the limit cycle attractor is nearly zero.

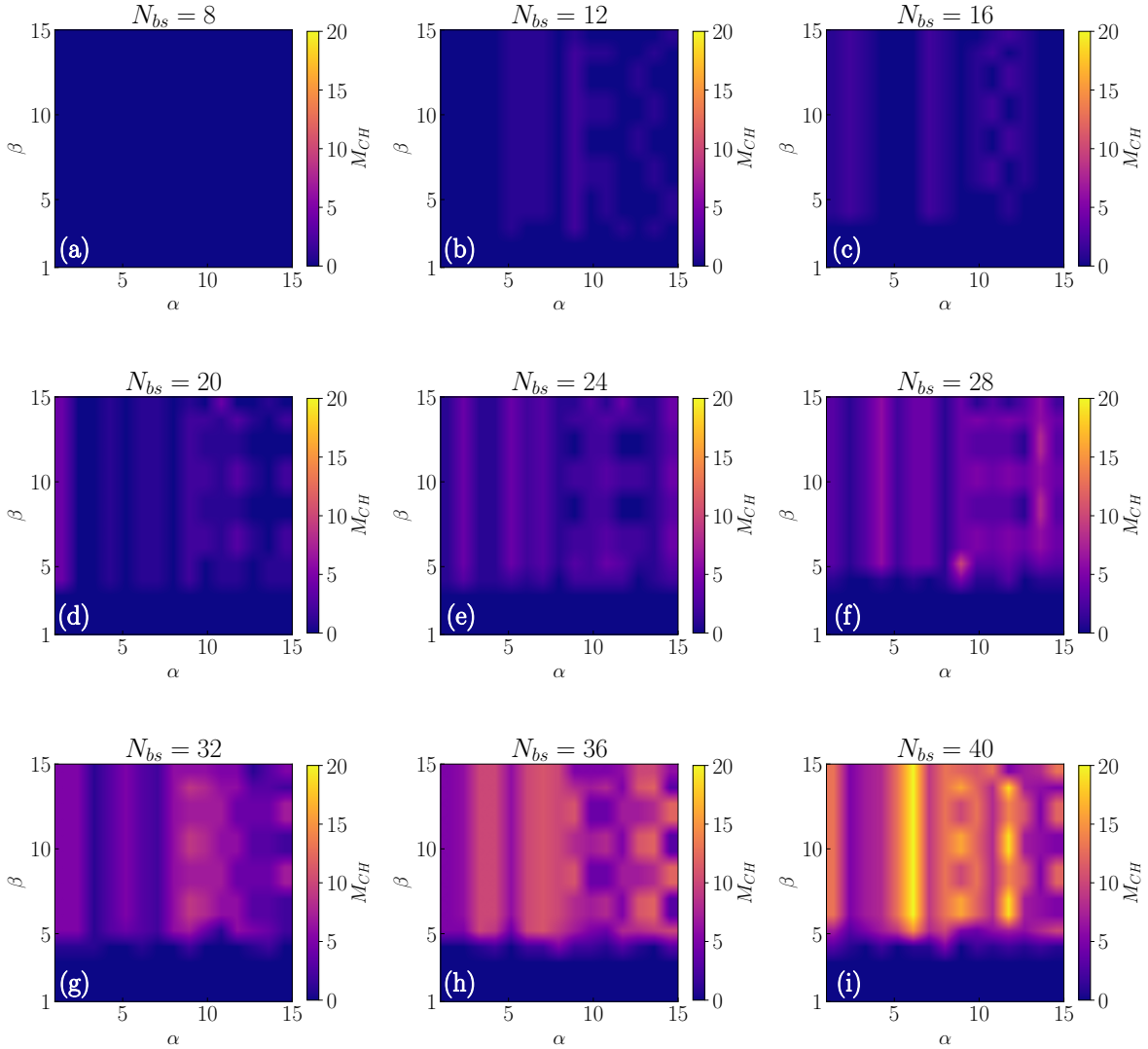


Figure 13: Influence of α and β on basin stability of chatter cutting for various values of the number of basis functions N_{bs} .

The heat-maps in Figs. 13 (b)-(i) reveal that the number of samples transitioning to chatter vibrations M_{CH} begins to rise as the number of basis functions N_{bs} increases. This rise reflects how enhanced initial surface irregularities (represented by the history function) can affect the stability of the tool's motion, increasing its susceptibility to noise. However, when the initial tool vibration amplitude constraint β is below 4, none of the simulations converged to the chatter limit cycle attractor, regardless of the specific α and N_{bs} values. This indicates that one can suppress the noise-induced transition, especially in regions exhibiting multi-stability. Moreover, as N_{bs} increases, there is a consistent upward trend in the number of samples that end up in the sticking limit cycle attractor. This highlights the importance of surface complexity in pushing the system towards the chatter limit cycle. The other notable observation from Fig. 13 (i) is the abrupt rise in M_{CH} at $\beta = 5$, jumping from zero to a maximum value of 20. This sudden change underscores the system's sensitivity to initial tool vibrations and the need for extra care in tool-workpiece interaction, particularly under stochastic conditions.

5.2 Entropy measures

Basin stability analysis provides the long-term stability structure of the system for a given initial workpiece profile. However, it is also important to compute the entropy measures to analyze the complexity and regularity of the noisy fluctuations in non-chatter, chatter, and multi-stable regimes. This section introduces and compares the result from several widely used entropy measures, namely, (a) Shannon entropy, (b) Conditional entropy, (c) Permutation entropy, (d) Approximate entropy, (e) Sample entropy, and (f) Fuzzy entropy, each with distinct advantages in capturing features of given noisy data. All the entropy measures were computed using the comprehensive set of MATLAB routines provided in Ref. [57]. Fig. 14 shows the results of entropy measures. Fig. 14 (a) represents the values of Shannon entropy (H_{SHE}) over the depth of cut values (a_p). Shannon entropy measures how much information is contained in the given signal [58, 59]. From Fig. 14 (a), it is clear that the H_{SHE} fluctuates between 0 and 3 in the chatter-free region and settles around 4 in the chatter region. Also, it reaches a peak near $a_p = 0.54 \text{ mm}$ at the onset of the multi-stable region (shaded portion in the figure). This change in the H_{SHE} values is likely due to the presence of coexisting attractors, which increases the signal's unpredictability and complexity. The elevated entropy reflects the dynamical competition between the two attractors at the multi-stable zone. Fig. 14 (b) presents the results of conditional entropy. It quantifies the remaining uncertainty about the future state of a system given knowledge of its past states [59]. It is clear from Fig. 14 (b) that the conditional entropy (H_{CE}) has values ranging from 0.01 to 0.5 in the non-chatter region and 0.2 to 0.22 in the multi-stable region. A low H_{CE} value indicates that the future state of the system is more predictable when the past states are known. Although only a fixed point attractor has been observed in the chatter-free region, noise alters the dynamics, causing the entropy values to oscillate. In the multi-stable and chatter region, the value is around 0.2 due to the system's periodic behavior.

Fig. 14 (c) illustrates the results of permutation entropy (H_{PE}) measurement. Permutation entropy quantifies the complexity of a given signal or disorderliness based on its values' ordinal patterns [60]. A high value of H_{PE} indicates high randomness of the signal. The permutation values in the chatter-free region are high when compared to the chatter and multi-stable regions. This is because added noise influences the patterns of the fixed point attractor in the chatter-free regions. Also, from Fig. 14 (c), it is observed that the H_{PE} values reach the minima at the beginning of the multi-stable region, indicating the occurrence of high amplitude transitions between the underlying stable states.

Fig. 14 (d) shows the values of approximate entropy (H_{AE}) computed varying the depth of cut value. Approximate entropy quantifies the amount of regularity in the given data [61]. This metric increases as a_p increases in the stochastic fixed point regime. In the chatter-free region, H_{AE} is around 0.1. However, it has the maximum value at the end of the chatter-free region, indicating that the system's predictability is very low near the multi-stable region. The reason for this is the co-existence of the two attractors, which affects the regularity of the time histories for the corresponding a_p values. Further, the H_{AE} values started to decrease and settled around 0.02 after the chatter-free region, indicating that even though only high amplitude chatter vibrations were observed for a_p from 0.61 to 1.2 mm, the dynamics of the system are not much affected by the included noise for that region. Thus, one observes fewer transitions from the stochastic limit cycle to the fixed point regime.

Fig. 14 (e) shows the results of sample entropy (H_{SE}) calculations. Sample entropy was introduced as an improvement over approximate entropy. It eliminates self-matching bias and has better relative consistency. Thus, a lower value of H_{SE} indicates more self-similarity in the time series [62]. It is clear from Fig. 14 (e) that H_{SE} has the maximum value of 2 in the chatter-free region and starts to decrease until around $a_p = 0.5 \text{ mm}$, where the multi-stable region starts. Unlike approximate entropy, sample entropy shows no sudden jump to a higher value before entering the multi-stable region. This is due to the elimination of self-matching bias. It has the same values as the approximate entropy results for the chatter region. Fig. 14 (f) represents the fuzzy entropy calculations. Fuzzy entropy (H_{FE}) uses the concept of fuzzy sets, utilizing an exponential function to assess the vector similarity more smoothly instead of using a hard threshold [63]. In this case, a trend similar to that of sample entropy has been observed, as sketched in Fig. 14 (f).

It is also worth noting that Figs. 14 (a) & (b), of Shannon entropy and the approximate entropy give contradictory results, *i.e.*, the value of H_{SHE} is higher in chatter region than in the chatter-free region whereas in the approximate entropy calculations, chatter-free region has the higher value of H_{AE} than in the chatter region. This is due to the nature of the entropy itself. When H_{AE} is low and H_{SHE} is high, it means that local patterns are regular, while the signal is globally diverse and random. The same behavior is observed when the results are compared between distribution-based (H_{SHE} and H_{CE}) and pattern-based (H_{AE} , H_{SE} , and H_{FE}) entropy measurements which indicate that the introduced noise has more effect in the non-chatter region than in chatter region.

6 Conclusion

This study proposes a model of an orthogonal metal cutting process combining regenerative, nonsmooth frictional, and stochastic effects. The role of nonsmooth friction in modelling the cutting system and predicting its stability is

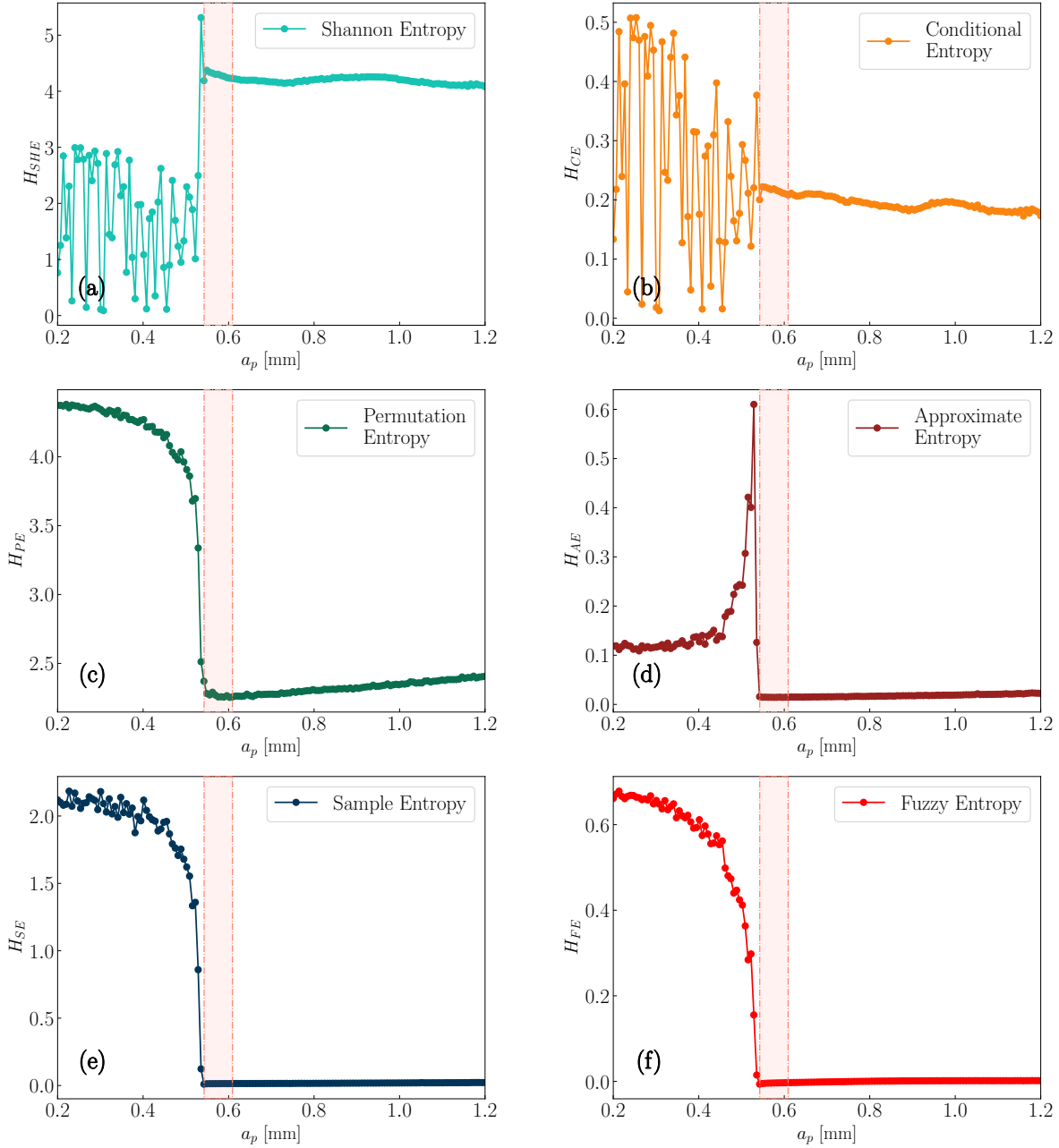


Figure 14: Various entropy measures. (a) Shannon entropy, (b) Conditional entropy, (c) Permutation entropy, (d) Approximate entropy, (e) Sample entropy, and (f) Fuzzy entropy. The shaded portion in all figures indicates the multi-stable zone from the deterministic study.

demonstrated through stability lobe diagrams obtained from a numerical continuation scheme. The proposed stochastic model demonstrates noise-induced transitions between stable fixed-point cutting and sticking limit-cycle oscillations associated with chatter vibrations. Stochastic P -bifurcations as well as D -bifurcations are observed to occur in the vicinity of the bi-stable region in the parameter space when the depth of cut is varied. The occurrence of P -bifurcations is numerically quantified by a sudden expansion of the area under the j -pdf at a designated level of probability, as the bifurcation parameter is varied. This area is numerically computed using the kernel density estimates. Lyapunov exponents are computed in the weak sense by evaluating the growth rates of perturbations using the first statistical moment, specifically the ensemble-averaged expectation. The results of the stochastic bifurcation study revealed that

the *P*-bifurcations and *D*-bifurcations occur at two distinct values of the parameter space. *P*-bifurcation occurred when the depth of cut was 0.54 mm, whereas the *D*-bifurcation occurred when the depth of cut was 0.53 mm, despite being computationally computed at the same step size of 0.001. This indicates that even though, in the averaged sense, the Lyapunov exponents can be negative, there could be a non-zero probability with which the orbit instantaneously transits to the other attractor.

Additionally, stability analysis of the stochastic attractors is carried out via two approaches, namely, basin stability and entropy measures. The basin stability analysis was carried out by considering history functions as sums of multiple harmonics generated via Fourier series expansions to incorporate the waviness of the initial workpiece surface and tool vibrations. The results of this analysis revealed that controlling chatter vibration is strongly linked to the magnitude of the initial tool vibrations. When the initial tool displacement constraint parameter was set to $\beta < 4$, the system maintained stable cutting regardless of the other constraint parameter, α , which is related to the workpiece surface. For values $\beta \geq 4$, the chance of entering the chatter zone increased by 25% to 100% depending on the parameter value α and the number of basis functions of the Fourier series. Various entropy measures, namely, Shannon entropy, conditional entropy, permutation entropy, approximate entropy, sample entropy, and fuzzy entropy, were systematically evaluated across varying depths of cut values from 0.2 to 1.2 mm. Each measure captured distinct facets of system complexity. It was observed that entropy values tend to be higher in the noisy fixed-point regime than in the noisy limit-cycle regime, highlighting an inherent periodicity within the chatter-dominated behavior.

Acknowledgments

The authors acknowledge the support from Sonic Research IT HPC Cluster from UCD, funding from UCD Chang' an Dublin International College of Transportation, Research Ireland 22/FFP/P11457 HarMonI, and Research Ireland funded I-Form Advanced Manufacturing Research Centre 1/RC/10295_P2.

Data Availability Statement

The data that supports the findings of this study are available within the article.

Appendix

A Stability lobes calculation

From Eq. (12),

$$\dot{y}_1(\tau) = y_2(\tau), \quad (26a)$$

$$\dot{y}_2(\tau) = -y_1(\tau) - \xi y_2(\tau) + W[\mu_{vs} \cos(\gamma) - \sin(\gamma)]h(\tau) - Wc_y \frac{y_2(\tau)}{n}, \quad (26b)$$

where

$$\mu_{vs} = \text{sign}(g) \left(\mu_d + (\mu_s - \mu_d)e^{|-g|} \right), \quad (27)$$

$$g = \frac{n}{v_s(\gamma, \phi)} - v \cos(\gamma) y_2(\tau), \quad (28)$$

$$\text{and } h(\tau) = 1 - y(\tau) + y(\tau - \tau_w). \quad (29)$$

For steady state,

$$(y_1(\tau), y_2(\tau)) \equiv (y_{10}, 0), \quad (30)$$

At the equilibrium chip thickness will be

$$h_0 = 1 - y_{10} + y_{10} = 1, \quad (31a)$$

$$g = \frac{n}{v_s} \quad (31b)$$

and the friction coefficient

$$\mu_{vs0} = \mu_d + (\mu_s - \mu_d) \exp\left(-\frac{n}{v_s}\right). \quad (31c)$$

Setting $\dot{y}_1 = \dot{y}_2 = 0$, from Eq. (26a),

$$\dot{y}_1 = \dot{y}_2 = 0$$

and from Eq. (26b),

$$y_{10} = W[\mu_{vs0} \cos(\gamma) - \sin(\gamma)]$$

substituting μ_{vs0} from Eq. (31c) which gives

$$y_{10} = W \left[\mu_d + (\mu_s - \mu_d) \exp\left(-\frac{n}{v_s}\right) \right] \cos(\gamma) - W \sin(\gamma). \quad (32)$$

The next step is to linearize the system around the equilibrium. Let the system be perturbed slightly from equilibrium:

$$y_1(\tau) = y_{10} + \delta y_1(\tau), \quad y_2(\tau) = 0 + \delta y_2(\tau), \quad (33)$$

where δy_1 and δy_2 are small perturbations. From Eq. (26a)

$$\delta \dot{y}_1 = \delta y_2, \quad (34)$$

and from Eq. (26b)

$$\delta \dot{y}_2 = -(y_{10} + \delta y_1) - \xi \delta y_2 + W(\mu_{vs} \cos(\gamma) - \sin(\gamma))h(\tau) - W c_y \frac{\delta y_2}{n}. \quad (35)$$

Substituting perturbations in chip thickness gives

$$h(\tau) = 1 - \delta y_1 + \delta y_1(\tau - \tau_w). \quad (36)$$

The friction coefficient depends on the velocity, so using the Taylor series to linearize it around $y_2 = 0$ gives

$$\mu_{vs} \approx \mu_{vs0} + \left. \frac{\partial \mu_{vs}}{\partial y_2} \right|_{y_2=0} \delta y_2 + \mathcal{O}(\delta y_2^2), \quad (37)$$

where

$$\left. \frac{\partial \mu_{vs}}{\partial y_2} \right|_{y_2=0} = \frac{\partial \mu_{vs}}{\partial g} \times \frac{\partial g}{\partial y_2} \quad (38)$$

$$\begin{aligned} \frac{\partial \mu_{vs}}{\partial g} &= \frac{\partial}{\partial g} [\text{sign}(g)(\mu_d + (\mu_s - \mu_d) \exp(-|g|))] \\ &= \frac{\partial}{\partial g} [\text{sign}(g)(\mu_s - \mu_d) \exp(-|g|)] \end{aligned}$$

Case 1: $g > 0 \rightarrow \text{sign}(g) = +ve$ and $|g| = g$

$$\begin{aligned} \frac{\partial \mu_{vs}}{\partial g} &= \frac{\partial}{\partial g} [+(\mu_s - \mu_d) \exp(-g)], \\ &= -(\mu_s - \mu_d) \exp(-g), \\ &= -(\mu_s - \mu_d) \exp(-|g|). \end{aligned} \quad (39a)$$

Case 2: $g < 0 \rightarrow \text{sign}(g) = -ve$ and $|g| = -g$

$$\begin{aligned} \frac{\partial \mu_{vs}}{\partial g} &= \frac{\partial}{\partial g} [-(\mu_s - \mu_d) \exp(g)], \\ &= -(\mu_s - \mu_d) \exp(g), \\ &= -(\mu_s - \mu_d) \exp(-|g|). \end{aligned} \quad (39b)$$

$$\left. \frac{\partial g}{\partial y_2} \right|_{y_2=0} = -v \cos(\gamma). \quad (40)$$

Substituting Eqs. (39) and (40) into Eq. (38), yields the partial derivative of the form

$$\begin{aligned} \left. \frac{\partial \mu_{vs}}{\partial y_2} \right|_{y_2=0} &= (\mu_s - \mu_d) v \cos(\gamma) \exp(-|[g]_{y_2=0}|) \delta y_2, \\ \left. \frac{\partial \mu_{vs}}{\partial y_2} \right|_{y_2=0} &= (\mu_s - \mu_d) v \cos(\gamma) \exp\left(-\frac{n}{v_s}\right) \delta y_2. \end{aligned} \quad (41)$$

Inserting the resulting partial derivative from Eq. (41) and μ_{vs0} from Eq. (31c) into Eq. (37), yields the linearized friction coefficient of the form

$$\mu_{vs} \approx \mu_d + (\mu_s - \mu_d) \exp\left(-\frac{n}{v_s}\right) (1 + v \cos(\gamma) \delta y_2) \quad (42)$$

Substituting Eqs. (32) and (42) into Eq. (35), followed by simplification and omission of second-order terms, yields an equation of the form

$$\delta \dot{y}_2 = -(1 + Wa) \delta y_1(\tau) - (\xi + Wb) \delta y_2(t) + Wa \delta y_1(\tau - \tau_w), \quad (43a)$$

For convenience, redefining δy as y

$$\dot{y}_2 = -(1 + Wa)y_1(\tau) - (\xi + Wb)y_2(t) + Way_1(\tau - \tau_w), \quad (43b)$$

where

$$a = \left(\mu_d + (\mu_s - \mu_d) \exp\left(-\frac{n}{v_s}\right) \right) \cos(\gamma) - \sin(\gamma), \quad (44a)$$

$$b = \frac{c_y}{n} + (\mu_d - \mu_s) \gamma \cos^2(\gamma) \exp\left(-\frac{n}{v_s}\right). \quad (44b)$$

Rearranging in matrix form

$$\dot{\mathbf{y}}(\tau) = \mathbf{A}\mathbf{y}(\tau) + \mathbf{D}\mathbf{y}(\tau - \tau_w), \quad (45)$$

where

$$\mathbf{y} = \begin{pmatrix} y_1 \\ y_2 \end{pmatrix}, \mathbf{A} = \begin{pmatrix} 0 & 1 \\ -(1 + Wa) & -(\xi + Wb) \end{pmatrix}, \mathbf{D} = \begin{pmatrix} 0 & 0 \\ Wa & 0 \end{pmatrix} \quad (46)$$

The stability is then determined by the eigenvalues of the following characteristic equation.

$$\det(\lambda \mathbf{I} - \mathbf{A} - \mathbf{D}e^{-\lambda \tau_w}) = 0, \quad (47)$$

Substituting $\lambda = \pm i\omega$ in Eq. (47) and separating the real and imaginary parts gives the equations of the following form

$$\omega^2 - 1 - Wa[1 - \cos(\omega \tau_w)] = 0, \quad (48a)$$

$$\omega(\xi + Wb) + Wa \sin(\omega \tau_w) = 0. \quad (48b)$$

B Numerical continuation scheme

Eq. (48) is transcendental without an analytical solution. It is solved numerically using the scheme given in [43]. A detailed description of how the critical equations, Eq. (48), are solved is provided below. It begins by performing a systematic seed-finding sweep over spindle speed and frequency ranges for a fixed value of depth of cut. Each valid intersection with a fixed depth-of-cut value serves as a starting point for continuation.

From these seeds, the algorithm traces entire stability boundaries using an arc-length predictor–corrector method, ensuring smooth traversal of folds and turning points. The resulting curves are then converted to a dimensional form, sorted, filtered, and intersected to extract the upper envelope. This final envelope forms the complete stability lobe diagram. It is worth noting that this continuation method performs effectively for equations without nonsmoothness, as it smoothly follows the solution branch by appropriately adjusting the relaxation parameter.

Require: Physical parameters:

$$\{m, c, \xi, k, K, c_y, R, H_D, \gamma, \phi, v_s, v, \mu_d, \mu_s\}$$

▷ Model data

Require: Continuation parameters:

inc

▷ Initial Predictor Step

rat

▷ Continuation Ratio

maxC

▷ Max points per curve

maxT

▷ Second-point attempts

$\|F\|_{\text{tol}}$

▷ Residual tolerance

dup_{tol}

▷ Duplicate tolerance

Require: $\bar{n} = [n_{\min}, n_{\max}, \Delta n]$, $\bar{\omega} = [\omega_{\min}, \omega_{\max}, \Delta \omega]$

▷ Search grid

Require: W^* ▷ Fixed value of W

{Phase 1: Generate raw solution curves via arc-length continuation}

```

1: CriticalEq( $\omega, W, n$ ): ▷ Function: Critical equations
2:    $a(n) = (\mu_d + (\mu_s - \mu_d)e^{-n/v_s}) \cos \gamma - \sin \gamma$ 
3:    $b(n) = c_y/n + (\mu_d - \mu_s)v \cos^2 \gamma \cdot e^{-n/v_s}$  ▷  $a$  and  $b$  coefficients
4:    $\tau_w = 60/n$ 
5:    $F_1(\omega, W, n) = \omega^2 - 1 - W \cdot a(n) \cdot (1 - \cos(\omega \tau_w))$ 
6:    $F_2(\omega, W, n) = \omega(\xi + W \cdot b(n)) + W \cdot a(n) \cdot \sin(\omega \tau_w)$ 
7:
8: return [ $F_1, F_2$ ]

9: Sol_System(F, guess, var, fixed): ▷ Function: Nonlinear solver
10:  $\mathbf{x} \leftarrow$  vector from guess[var] ▷ Initial iterate
11: repeat
12:   Build dictionary  $sol$  from ( $var, \mathbf{x}$ ) ▷ Insert free variables
13:   if fixed  $\neq$  None then
14:      $sol \leftarrow sol \cup$  fixed ▷ Inject fixed parameters
15:   end if
16:    $R \leftarrow F(sol)$  ▷ Evaluate residual
17:   if  $\|R\| < \|F\|_{tol}$  then
18:     return  $sol$  ▷ Converged
19:   end if
20:    $J \leftarrow$  finite-difference Jacobian of  $F$  ▷ Numerical derivative
21:   Solve  $J \Delta x = -R$  ▷ Newton step
22:    $x \leftarrow x + \Delta x$  ▷ Update iterate
23: until max iterations reached
24: return NULL ▷ No convergence (reject)

25: Calc_Seed( $F, W^*, \bar{n}, \bar{\omega}$ ): ▷ Function: Seed finding
26:  $S \leftarrow \emptyset$  ▷ Initialize list
27: for  $n_0 \in [n_{min}, n_{max}]$  (nstep) do
28:   for  $\omega_0 \in [\omega_{min}, \omega_{max}]$  ( $\omega$ step) do
29:     guess  $\leftarrow \{n : n_0, \omega : \omega_0, W : W^*\}$  ▷ Build initial guess
30:     sol  $\leftarrow$  Sol_System( $F, guess, [n, \omega], \{W : W^*\}$ ) ▷ Newton solve
31:     if sol  $\neq$  NULL and  $n, \omega \in \mathbb{R}$  and  $n \in [n_{min}, n_{max}]$  and  $\omega > 0$  then
32:        $S.append(sol)$  ▷ Accept valid seed
33:     end if
34:   end for
35: end for

36: Remove duplicates:  $\|s_i - s_j\| < 10^{-12}, s \in S$  ▷ Clean seed set
37:
38: return  $S$  ▷ All ( $n, \omega$ ) solutions at  $W^*$ 

39: ArcConti( $F, W^*, \bar{n}, \bar{\omega}, S, inc, rat, maxC, maxT$ ): ▷ Function: Arc-length continuation
40:  $S\_Curves \leftarrow \emptyset, varAll = [n, \omega, W]$  ▷ Init
41: for  $S_0 \in S$  do
42:   sols  $\leftarrow S_0, ratio \leftarrow rat$  ▷ Start new curve
43:   Find 2nd point
44:   for  $k = 0$  to  $maxT - 1$  do
45:      $\delta W_k \leftarrow inc/2^k$  ▷ Shrinking step
46:     guess2[ $W$ ]  $\leftarrow W^* + \delta W_k$ 
47:     sol2  $\leftarrow$  Sol_System( $F, guess2, [n, \omega], \{W : W^* + \delta W_k\}$ ) ▷ Newton solve
48:     if  $\|F(sol2)\| < 10^{-10}$  then
49:       sols.append(sol2)
50:       break ▷ Accept 2nd point
51:     end if
52:   end for
53:   Main loop
54:   for step = 1 to  $maxC$  do

```

```

55:    $s_1 \leftarrow \text{sols}[-2], \quad s_2 \leftarrow \text{sols}[-1]$ 
56:    $\mathbf{v}_1 = [s_1.n, s_1.\omega, s_1.W], \quad \mathbf{v}_2 = [s_2.n, s_2.\omega, s_2.W]$ 
57:    $\mathbf{v}_g \leftarrow (1 + \text{ratio})\mathbf{v}_2 - \text{ratio}\mathbf{v}_1$ 
58:   eq_aug(sol):
59:    $x \leftarrow [\text{sol}[n], \text{sol}[\omega], \text{sol}[W]]$ 
60:   ortho  $\leftarrow (x - v_g) \cdot (v_g - v_2)$ 
61:   return  $[F_1(\text{sol}), F_2(\text{sol}), \text{ortho}]$ 
62:   sol  $\leftarrow \text{Sol\_System}(\text{eq\_aug}, \mathbf{v}_g, \text{varAll})$ 
63:   if sol = NULL then
64:     ratio  $\leftarrow \text{ratio} / \text{rat}$ 
65:     continue
66:   end if
67:   sols.append(sol)
68:   ratio  $\leftarrow \text{rat}$ 
69:   if  $n \notin [n_{\min}, n_{\max}]$  then
70:     break
71:   end if
72: end for
73: S_Curves.append(sols)
74: end for
75:
76: return S_Curves
    
```

▷ Predictor
 ▷ Augmented system for corrector
 ▷ Current iterate
 ▷ Orthogonality constraint
 ▷ 3×3 augmented system
 ▷ Corrector
 ▷ Reduce step
 ▷ Reset step size
 ▷ Curve completed
 ▷ Store completed curve
 ▷ All continuation curves

{Phase 2: Lobe envelope construction}

```

77: Dimensional conversion:
78:  $N \leftarrow n \sqrt{k/m}$ 
79:  $a_p \leftarrow W \frac{k}{K} 10^3$ 
80: Step 1:
81:  $i_{\min} \leftarrow \arg \min_j a_{p,i}(N_j)$  for all curves  $\mathcal{C}_i$ 
82: Step 2:
83: Sort curves by  $N[i_{\min}]$  ascending
84: Step 3:
85: Remove curves where  $a_{p,i}(N_k) < a_{p,j}(N_k) + \varepsilon$  for all common  $N_k$ 
86: Step 4:
87: If a lobe has  $N_0 > N_{\text{end}}$ , reverse its arrays
88: Step 5:
89: For each adjacent pair  $(i, i + 1)$  solve  $a_{p,i}(N) = a_{p,i+1}(N)$ 
90: Step 6:
91: Cut each lobe at its intersection with the next
92:
93: return SLD
    
```

▷ Convert to physical units
 ▷ Spindle speed (RPM)
 ▷ Depth of cut (mm)
 ▷ Identify minima of each curve
 ▷ Sort lobes left→right
 ▷ Remove dominated lobes
 ▷ Ensure increasing N
 ▷ Compute lobe intersections
 ▷ Trim upper envelope
 ▷ Final stability lobe diagram

References

- [1] M. Bernardo, C. Budd, A. R. Champneys, P. Kowalczyk, Piecewise-smooth dynamical systems: theory and applications, volume 163, Springer Science & Business Media, 2008.
- [2] K. Popp, Non-smooth mechanical systems, Journal of Applied Mathematics and Mechanics 64 (2000) 765–772.
- [3] W. Chin, E. Ott, H. E. Nusse, C. Grebogi, Grazing bifurcations in impact oscillators, Physical Review E 50 (1994) 4427.
- [4] M. Wiercigroch, Applied nonlinear dynamics of non-smooth mechanical systems, Journal of the Brazilian Society of Mechanical Sciences and Engineering 28 (2006) 519–526.
- [5] E. Ozturk, Want to save costs and be more sustainable? stop the chatter, <https://www.amrc.co.uk/news>, 2023. Accessed: 2025-08-23.
- [6] M. Wiercigroch, A. M. Krvitsov, Frictional chatter in orthogonal metal cutting, Philosophical Transactions of the Royal Society of London. Series A: Mathematical, Physical and Engineering Sciences 359 (2001) 713–738.

- [7] R. Rusinek, M. Wiercigroch, P. Wahi, Modelling of frictional chatter in metal cutting, *International Journal of Mechanical Sciences* 89 (2014) 167–176.
- [8] P. Wahi, A. Chatterjee, Self-interrupted regenerative metal cutting in turning, *International Journal of Non-Linear Mechanics* 43 (2008) 111–123.
- [9] G. Stépán, Modelling nonlinear regenerative effects in metal cutting, *Philosophical Transactions of the Royal Society of London. Series A: Mathematical, Physical and Engineering Sciences* 359 (2001) 739–757.
- [10] X. Zhang, L. Wan, X. Ran, Research progress on the chatter stability in machining systems, *The International Journal of Advanced Manufacturing Technology* 131 (2024) 29–62.
- [11] M. Wiercigroch, E. Budak, Sources of nonlinearities, chatter generation and suppression in metal cutting, *Philosophical Transactions of the Royal Society of London. Series A: Mathematical, Physical and Engineering Sciences* 359 (2001) 663–693.
- [12] Z. Dombovari, D. A. Barton, R. E. Wilson, G. Stepan, On the global dynamics of chatter in the orthogonal cutting model, *International Journal of Non-Linear Mechanics* 46 (2011) 330–338.
- [13] K. Engelborghs, T. Luzyanina, G. Samaey, DDE-BIFTOOL v. 2.00: a matlab package for bifurcation analysis of delay differential equations (2001).
- [14] W. Bai, R. Sun, A. Roy, V. V. Silberschmidt, Improved analytical prediction of chip formation in orthogonal cutting of titanium alloy ti6al4v, *International Journal of Mechanical Sciences* 133 (2017) 357–367.
- [15] G. Gyebrószki, D. Bachrathy, G. Csernák, G. Stepan, Stability of turning processes for periodic chip formation, *Advances in Manufacturing* 6 (2018) 345–353.
- [16] K. Ahmadi, Analytical investigation of machining chatter by considering the nonlinearity of process damping, *Journal of Sound and Vibration* 393 (2017) 252–264.
- [17] M. Eynian, Y. Altintas, Chatter stability of general turning operations with process damping, *Journal of Manufacturing Science and Engineering* 131 (2009) 041005.
- [18] B. Yuvaraju, J. Srinivas, B. Nanda, Nonlinear dynamics of friction-induced regenerative chatter in internal turning with process damping forces, *Journal of Sound and Vibration* 544 (2023) 117386.
- [19] Y. Altintas, M. Weck, Chatter stability of metal cutting and grinding, *CIRP annals* 53 (2004) 619–642.
- [20] H. Li, Y. C. Shin, A study on chatter boundaries of cylindrical plunge grinding with process condition-dependent dynamics, *International Journal of Machine Tools and Manufacture* 47 (2007) 1563–1572.
- [21] Y. Yan, J. Xu, M. Wiercigroch, Chatter in a transverse grinding process, *Journal of Sound and Vibration* 333 (2014) 937–953.
- [22] Y. Yan, J. Xu, M. Wiercigroch, Stability and dynamics of parallel plunge grinding, *The International Journal of Advanced Manufacturing Technology* 99 (2018) 881–895.
- [23] T. Liu, W. Li, Z. Deng, Q. Yao, J. Tang, J. Yan, H. Kang, Chatter stability analysis for non-circular high-speed grinding process with dynamic force modelling, *Journal of Sound and Vibration* 595 (2025) 118782.
- [24] J. C. Roukema, Y. Altintas, Generalized modeling of drilling vibrations. part ii: Chatter stability in frequency domain, *International Journal of Machine Tools and Manufacture* 47 (2007) 1474–1485.
- [25] J. C. Roukema, Y. Altintas, Generalized modeling of drilling vibrations. part i: Time domain model of drilling kinematics, dynamics and hole formation, *International Journal of Machine Tools and Manufacture* 47 (2007) 1455–1473.
- [26] E. Stone, S. A. Campbell, Stability and bifurcation analysis of a nonlinear dde model for drilling, *Journal of Nonlinear Science* 14 (2004) 27–57.
- [27] G. Wang, H. Dong, Y. Guo, Y. Ke, Chatter mechanism and stability analysis of robotic boring, *The International Journal of Advanced Manufacturing Technology* 91 (2017) 411–421.
- [28] Y. Altintas, G. Stépán, D. Merdol, Z. Dombóvári, Chatter stability of milling in frequency and discrete time domain, *CIRP Journal of Manufacturing Science and Technology* 1 (2008) 35–44.
- [29] T. Insperger, G. Stépán, P. Bayly, B. Mann, Multiple chatter frequencies in milling processes, *Journal of sound and vibration* 262 (2003) 333–345.
- [30] L. Zhu, C. Liu, Recent progress of chatter prediction, detection and suppression in milling, *Mechanical Systems and Signal Processing* 143 (2020) 106840.
- [31] Y. Altintas, G. Stepan, E. Budak, T. Schmitz, Z. M. Kilic, Chatter stability of machining operations, *Journal of Manufacturing Science and Engineering* 142 (2020) 110801.

- [32] G. Quintana, J. Ciurana, Chatter in machining processes: A review, *International Journal of Machine Tools and Manufacture* 51 (2011) 363–376.
- [33] M. Siddhpura, R. Paurobally, A review of chatter vibration research in turning, *International Journal of Machine tools and manufacture* 61 (2012) 27–47.
- [34] W. Sujuan, Z. Tao, D. Wenping, S. Zhanwen, S. To, Analytical modeling and prediction of cutting forces in orthogonal turning: a review, *The international journal of advanced manufacturing technology* (2021) 1–28.
- [35] G. Fodor, H. T. Sykora, D. Bachrathy, Stochastic modeling of the cutting force in turning processes, *The International Journal of Advanced Manufacturing Technology* 111 (2020) 213–226.
- [36] P. Kumar, S. Narayanan, S. Gupta, Bifurcation analysis of a stochastically excited vibro-impact duffing-van der pol oscillator with bilateral rigid barriers, *International Journal of Mechanical Sciences* 127 (2017) 103–117.
- [37] R. C. Hilborn, *Chaos and nonlinear dynamics: an introduction for scientists and engineers*, Oxford university press, 2000.
- [38] L. Arnold, N. Sri Namachchivaya, K. R. Schenk-Hoppé, Toward an understanding of stochastic hopf bifurcation: a case study, *International Journal of Bifurcation and Chaos* 6 (1996) 1947–1975.
- [39] E. Buckwar, R. Kuske, B. L'esperance, T. Soo, Noise-sensitivity in machine tool vibrations, *International Journal of Bifurcation and Chaos* 16 (2006) 2407–2416.
- [40] J. Gradišek, I. Grabec, S. Siegert, R. Friedrich, Stochastic dynamics of metal cutting: bifurcation phenomena in turning, *Mechanical Systems and Signal Processing* 16 (2002) 831–840.
- [41] H. T. Sykora, D. Bachrathy, G. Stepan, A theoretical investigation of the effect of the stochasticity in the material properties on the chatter detection during turning, in: *International Design Engineering Technical Conferences and Computers and Information in Engineering Conference*, volume 58226, American Society of Mechanical Engineers, 2017, p. V008T12A054.
- [42] G. Fodor, D. Bachrathy, Efficient approximation of stochastic turning process based on power spectral density, *The International Journal of Advanced Manufacturing Technology* 133 (2024) 5673–5681.
- [43] Y. Yan, J. Xu, M. Wiercigroch, Modelling of regenerative and frictional cutting dynamics, *International Journal of Mechanical Sciences* 156 (2019) 86–93.
- [44] Y. Yan, G. Liu, M. Wiercigroch, J. Xu, Safety estimation for a new model of regenerative and frictional cutting dynamics, *International Journal of Mechanical Sciences* 201 (2021) 106468.
- [45] R. Kuske, Competition of noise sources in systems with delay: the role of multiple time scales, *Journal of Vibration and Control* 16 (2010) 983–1003.
- [46] A. Rounak, S. Gupta, Stochastic p-bifurcation in a nonlinear impact oscillator with soft barrier under ornstein–uhlenbeck process, *Nonlinear Dynamics* 99 (2020) 2657–2674.
- [47] D. Liu, M. Li, J. Li, Probabilistic response and analysis for a vibro-impact system driven by real noise, *Nonlinear Dynamics* 91 (2018) 1261–1273.
- [48] Y. Yan, J. Xu, M. Wiercigroch, Basins of attraction of the bistable region of time-delayed cutting dynamics, *Physical Review E* 96 (2017) 032205.
- [49] Y. Altintas, M. Eynian, H. Onozuka, Identification of dynamic cutting force coefficients and chatter stability with process damping, *CIRP annals* 57 (2008) 371–374.
- [50] L. F. Shampine, S. Thompson, Solving ddes in MATLAB, *Applied Numerical Mathematics* 37 (2001) 441–458.
- [51] D. Higham, P. Kloeden, *An introduction to the numerical simulation of stochastic differential equations*, SIAM, 2021.
- [52] H. Crauel, A. Debussche, F. Flandoli, Random attractors, *Journal of Dynamics and Differential Equations* 9 (1997) 307–341.
- [53] P. Sundqvist, Contour2Area, <https://www.mathworks.com/matlabcentral/fileexchange/26480-contour2area>, 2025. MATLAB Central File Exchange. Retrieved July 25, 2025.
- [54] H. Wernecke, B. Sándor, C. Gros, Chaos in time delay systems, an educational review, *Physics Reports* 824 (2019) 1–40.
- [55] P. Benardos, G.-C. Vosniakos, Predicting surface roughness in machining: a review, *International journal of machine tools and manufacture* 43 (2003) 833–844.
- [56] P. Belardinelli, S. Lenci, Improving the global analysis of mechanical systems via parallel computation of basins of attraction, *Procedia IUTAM* 22 (2017) 192–199.

- [57] J. Monge-Álvarez, A set of entropy measures for temporal series (1d signals), MATLAB Central File Exchange, 2014.
- [58] C. E. Shannon, A mathematical theory of communication, *The Bell system technical journal* 27 (1948) 379–423.
- [59] A. Porta, G. Baselli, D. Liberati, N. Montano, C. Cogliati, T. Gneccchi-Rusccone, A. Malliani, S. Cerutti, Measuring regularity by means of a corrected conditional entropy in sympathetic outflow, *Biological cybernetics* 78 (1998) 71–78.
- [60] C. Bandt, B. Pompe, Permutation entropy: a natural complexity measure for time series, *Physical review letters* 88 (2002) 174102.
- [61] S. M. Pincus, I. M. Gladstone, R. A. Ehrenkranz, A regularity statistic for medical data analysis, *Journal of clinical monitoring* 7 (1991) 335–345.
- [62] J. S. Richman, J. R. Moorman, Physiological time-series analysis using approximate entropy and sample entropy, *American journal of physiology-heart and circulatory physiology* 278 (2000) H2039–H2049.
- [63] W. Chen, Z. Wang, H. Xie, W. Yu, Characterization of surface emg signal based on fuzzy entropy, *IEEE Transactions on neural systems and rehabilitation engineering* 15 (2007) 266–272.